Application of a new image correction method for the First G-APD Cherenkov Telescope

---

von Thomas Bussek

Bachelorarbeit im Fach Physik

vorgelegt der

Fakultät für Mathematik, Informatik und Naturwissenschaften
der RWTH Aachen

im Oktober 2016

angefertigt am

III. Physikalischen Institut A

bei Prof. Dr. Thomas Bretz

Erstgutachter und Betreuer

Prof. Dr. Thomas Bretz
III. Physikalisches Institut A
RWTH Aachen

Zweitgutachter

Prof. Dr. Thomas Hebbeker
III. Physikalisches Institut A
RWTH Aachen

Eidesstattliche Versicherung

Name, Vorname

Matrikelnummer (freiwillige Angabe)

Ich versichere hiermit an Eides Statt, dass ich die vorliegende Arbeit/Bachelorarbeit/ Masterarbeit* mit dem Titel

selbständig und ohne unzulässige fremde Hilfe erbracht habe. Ich habe keine anderen als die angegebenen Quellen und Hilfsmittel benutzt. Für den Fall, dass die Arbeit zusätzlich auf einem Datenträger eingereicht wird, erkläre ich, dass die schriftliche und die elektronische Form vollständig übereinstimmen. Die Arbeit hat in gleicher oder ähnlicher Form noch keiner Prüfungsbehörde vorgelegen.

Ort, Datum

Unterschrift

*Nichtzutreffendes bitte streichen

Belehrung:

§ 156 StGB: Falsche Versicherung an Eides Statt

Wer vor einer zur Abnahme einer Versicherung an Eides Statt zuständigen Behörde eine solche Versicherung falsch abgibt oder unter Berufung auf eine solche Versicherung falsch aussagt, wird mit Freiheitsstrafe bis zu drei Jahren oder mit Geldstrafe bestraft.

§ 161 StGB: Fahrlässiger Falscheid; fahrlässige falsche Versicherung an Eides Statt

(1) Wenn eine der in den §§ 154 bis 156 bezeichneten Handlungen aus Fahrlässigkeit begangen worden ist, so tritt Freiheitsstrafe bis zu einem Jahr oder Geldstrafe ein.

(2) Straflosigkeit tritt ein, wenn der Täter die falsche Angabe rechtzeitig berichtigt. Die Vorschriften des § 158 Abs. 2 und 3 gelten entsprechend.

Die vorstehende Belehrung habe ich zur Kenntnis genommen:

Ort, Datum

Unterschrift

Abstract

The First G-APD Cherenkov Telescope (FACT) is an imaging atmospheric Cherenkov telescope built in 2011 on the Canary Island of La Palma. It is designated to establish the use of Geiger-mode avalanche photodiodes (G-APDs) which provide features towards the common used photomultiplier tubes.
Since the imaging properties of its reflector have immediate impact on the shower image and thus the overall spatial resolution of FACT, this influence has been studied recently and a new correction method was introduced.
This thesis deals with the implementation and the investigation of the impact of this new correction method. For this Monte Carlo simulations are used to prove the correct implementation by taking a closer look at the change of well predictable image parameters. Furthermore, the change of parameters used for the reconstruction of the source position are investigated, yielding an overall improvement of 1.87% for the resolution of FACT.

Kurzfassung

Das First G-APD Cherenkov Telescope (FACT) ist ein abbildendes, atmosphärisches Cherenkov Teleskop, das 2011 auf der kanarischen Insel Las Palmas gebaut wurde. Es soll die Nutzung von Geiger-Mode Lawinenphotodioden etablieren, die einige Vorteile gegenüber den häufig benutzten Photomultiplier-Röhren aufweisen.
Da die abbildenden Eigenschaften des Reflektors unmittelbaren Einfluss auf das genommene Schauerbild und somit die Auflösung von FACT haben, wurde dieser Einfluss kürzlich untersucht und eine entsprechende Bildkorrektur vorgestellt.
Diese Arbeit behandelt die Implementation und Untersuchung der Auswirkungen dieses Bildkorrekturverfahrens. Dazu werden Monte Carlo Simulationen genutzt, um die korrekte Implementation an gut vorhersagbaren Bildparametern zu zeigen. Des Weiteren wird die Änderung von Parametern, die zur Rekonstruktion der Quellposition genutzt werden, untersucht, was zu einer insgesamten Verbesserung der Auflösung von FACT um 1.87% führt.

Contents

1 Cosmic Rays

Cosmic rays, discovered in 1912 by Victor F. Hess, are energetic particles originating from outside the solar system with their exact sources still unknown. They are mainly composed of charged particles as nucleons and electrons but also neutral particles as gamma-rays, neutrinos and anti-neutrinos are part of cosmic rays [1, 2]. The cosmic ray energies cover a huge range from some keV up to more than 10^{11} GeV and can be subdivided into three parts. This is shown in Fig. 1.1 where the differential energy spectrum is shown. It can be described by the power law $dN/dE \propto E^{-\alpha}$ [3].

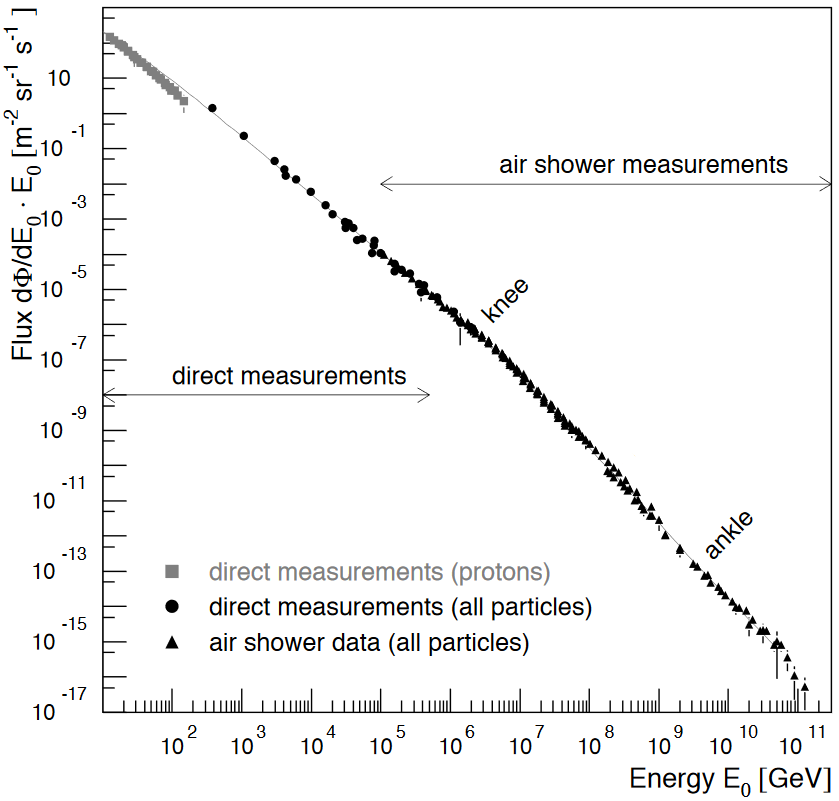

Fig. 1.1: Differential energy spectrum of galactic cosmic rays, direct and indirect measurements of several experiments combined [4].

The first area describes energies up to about $3 \cdot 10^6$ GeV with a spectral index α of 2.7 and is called the *knee* region. Particles with energies in this area are supposed to come from galactic sources [5].
The second corridor reaches from the *knee* at about $3 \cdot 10^6$ GeV to the *ankle* at about

10^9 GeV. The spectral index changes to $\alpha = 3.0$ in this area. This steepening is explained by galactic particles beginning to escape from the galaxy because the galactic magnetic field is not strong enough anymore to keep them captured [6].
Finally the *ankle* at about 10^9 GeV marks the beginning of the last region and is considered to be related to the transition from galactic to extra galactic sources [7].
It is expected to see a clear cutoff for energies above some 10^{11} GeV due to the so-called Greisen-Zatsepin-Kuzmin cutoff, which represents a limitation for the mean free-path of extreme high energy cosmic ray particles ($E > 10^{11}$ GeV). This limitation of some tens of mega-parsecs leads to the universe being opaque for particle energies above about 10^{11} GeV [8, 9].
As shown in Fig. 1.1 there are in principle two possible methods to investigate cosmic rays. The first one is using high-flying balloons or satellites in order to get detectors above or almost above the Earth's atmosphere, so that it has no or at least a negligible impact on incoming particles. With such experimental set-ups it is possible to detect cosmic rays directly. But for very high energy (VHE) particles larger detectors and longer observation times are needed in order to still get reasonable statistics as the overall flux drops rapidly (see Fig. 1.1). As a consequence this method is getting more and more expensive. Therefore, at about 10^5 GeV, it becomes necessary to detect the primary cosmic rays indirectly and build ground-based detectors covering huge areas up to some thousand km^2. By detecting secondary particles which are part of so-called extensive air showers (EASs) the properties of the primary particles can be reconstructed [10].

1.1 Extended air showers

An incoming VHE cosmic-ray typically first interacts with an Earth's atmosphere molecule at a height of about 20 - 25 km above sea level [7].The secondary particles originating from the first interaction interact again and thus a cascade of secondary particles emerges. The resulting EAS depends on several factors such as the energy of the incoming primary particle and most importantly the type of primary particle [2, 7].
That is useful because the different types of primary particles offer different advantages for research. In order to distinguish between the different kinds of incoming cosmic ray particles, primary particle dependent differences in the development of EASs need to be studied.

1.1.1 Electromagnetic showers

In general, a typical gamma-induced EAS starts by creating an electron and a positron by pair production. Both particles predominantly lose their energy by

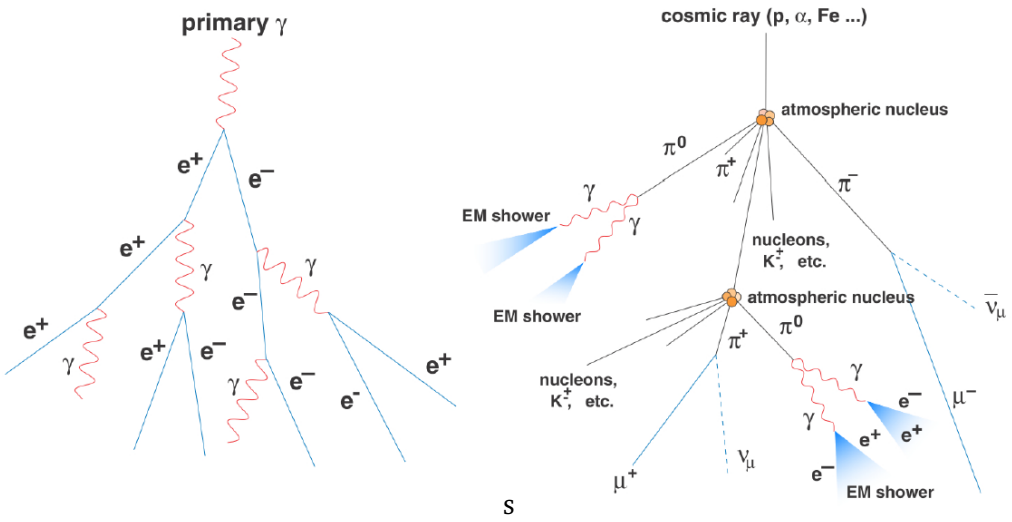

Fig. 1.2: Left: gamma-induced EAS. Right: hadron-induced EAS [7].

bremsstrahlung, thus they create new photons which may again cause pair production themselves until the energy drops below a certain level and the EAS starts to die out [11].
The positron and electron of the first pair production share the energy of the initial gamma-ray and travel almost in the same direction like the primary gamma-ray. All secondary particles of the EAS are radiated with an angle of emission which is proportional to m_e/E (E describes the electron energy, m_e its rest mass). Due to the low ratio between m_e and E, this angle is small and resulting EASs develop close to the axis of the incoming gamma-ray (see Fig. 1.2, left)) [2].

1.1.2 Hadronic showers

A hadron-induced EAS has a slightly different shower development than a gamma-ray induced one. In particular the interactions between high energetic incoming hadrons and the Earth's atmospheric molecules result in a larger number of secondary particles like pions, kaons and light baryons [7]. These secondary particles interact again with the atmosphere until they reach a critical energy level. Meanwhile the pions, which account for about 90% of the secondary particles [7], decay into muons or photons which may initiate electromagnetic sub-showers.
The secondary particles of such shower events feature a much higher transverse momentum in the order of 0.3 GeV/c and thus the EAS is more scattered and broader (see Fig. 1.2, right)).
Furthermore hadrons have a larger interaction length than gamma-rays, electrons and positrons. Therefore the shower maximums of hadronic showers are deeper in the atmosphere than those of electromagnetic showers [12].

2 Gamma-ray astronomy

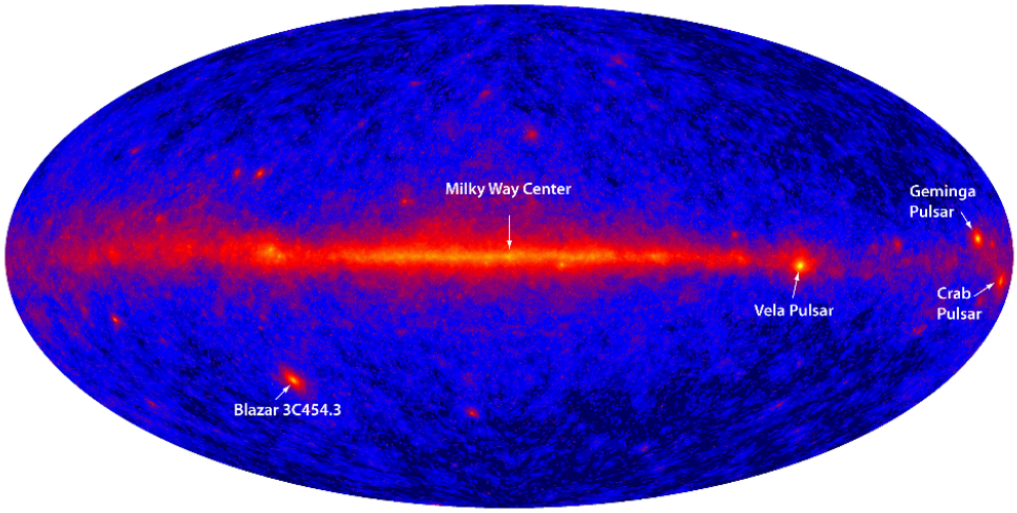

Fig. 2.1: All sky picture of the universe in GeV gamma-ray range, taken by the Fermi LAT. The Galactic plane and some bright sources are highlighted [11].

As mentioned in chapter 1, the origin of cosmic rays remains unknown and thus is a topic of current research. Charged primary cosmic rays are of no interest for extended research because they interact with intergalactic magnetic fields and hence are nearly isotropic distributed over the sky and not suitable for studying their sources [2].

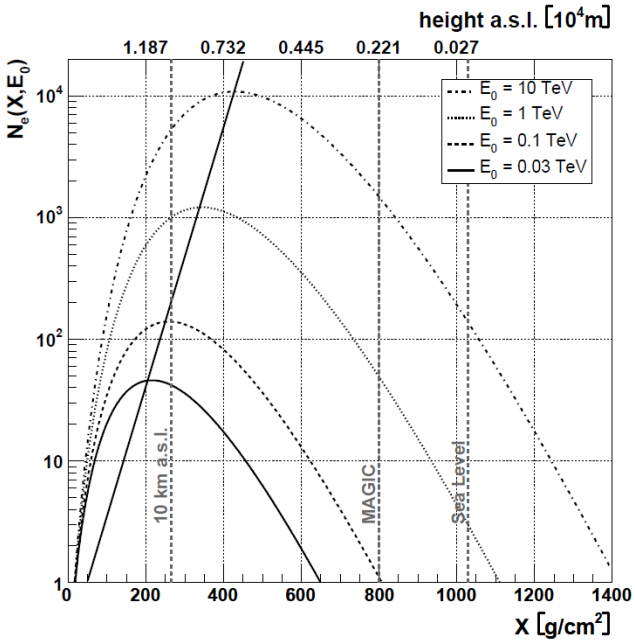

Fig. 2.2: Number of electrons above the critical energy E_C in an gamma-induced EAS, dependent of the primary energy and the atmospheric depth X. Straight line marks shower maximums [2].

X- and gamma-rays are not distorted by magnetic fields. The only potential disturbing effects are time dispersion and influences through gravitational lensing. Both effects seem to be negligible in comparison to the influence magnetic fields have on charged particles. Thus gamma-ray astronomy has become a very important topic in astrophysics and the recent research of the origin of cosmic

rays [11, 2].
The Earth's atmosphere shields most electromagnetic waves except for wavelengths of the optical and radio window. Therefore X-rays (keV-MeV) and low-energy gamma-rays (MeV-GeV) must be measured by detectors in outer space. But, as mentioned above, beyond energies of some 100 GeV, when the overall flux has dropped so far, that detectors in outer space are not able to produce reliable statistic data anymore, incoming VHE gamma-rays create EASs by interacting with the Earth's atmosphere. Investigating those EASs makes it possible to study the primary gamma-rays themselves. Most of the EASs die out before they can be measured by ground-based detectors, even if those detectors are built a few thousand meters above sea level like the MAGIC or the FACT detectors (see Fig. 2.2). Therefore it is useful to track the secondary particles of an EAS indirectly, which is possible by the "Cherenkov effect".

2.1 Cherenkov light

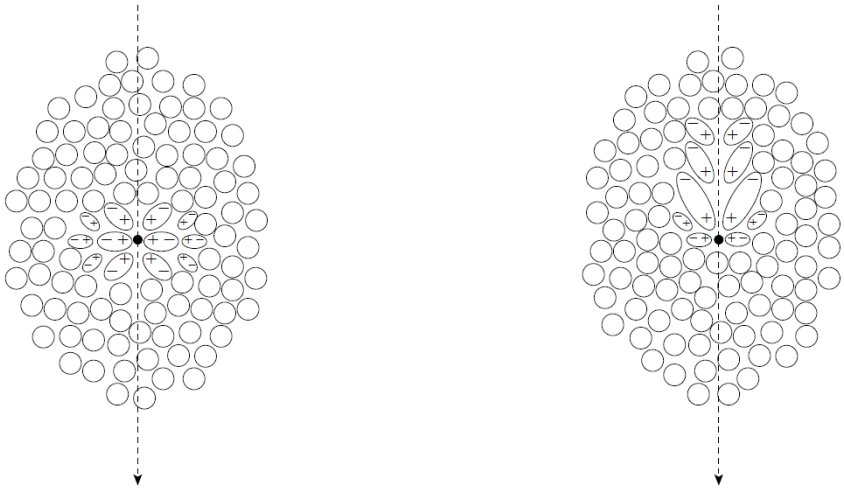

(a) The local polarization induced by a charged particle moving at a velocity $v < c/n$.

(b) The local polarization for a particle moving at superluminal velocity $v > c/n$.

Fig. 2.3: Local polarization of Earth's atmospheric molecules induced by a particle below and above the speed of light. Polarization is symmetrical for low velocities (a), for high velocities an overall dipole along the trajectory remains [2].

A charged particle traveling through a dielectric medium with a velocity greater than the phase velocity of light emits so-called Cherenkov photons.
Fig. 2.3 illustrates the underlying mechanism. The charged particle induces small dipole moments on nearby molecules. When the particle travels with a low velocity v these dipole moments are symmetrically orientated around the particle and thus cancel each other out on large scales (see Fig. 2.3, a)). At velocities faster than the speed of light in the corresponding dielectric medium this symmetry does not exist

anymore (see Fig. 2.3, b)).
That results in a remaining overall dipole moment which causes the molecules to emit Cherenkov photons [13]. Since those electromagnetic pulses are superpositioned they interfere with each other destructively except for the Cherenkov angle θ. Fig. 2.4 illustrates the underlying geometry.

$$cos(\theta) = \frac{1}{\beta \cdot n} \qquad (2.1)$$

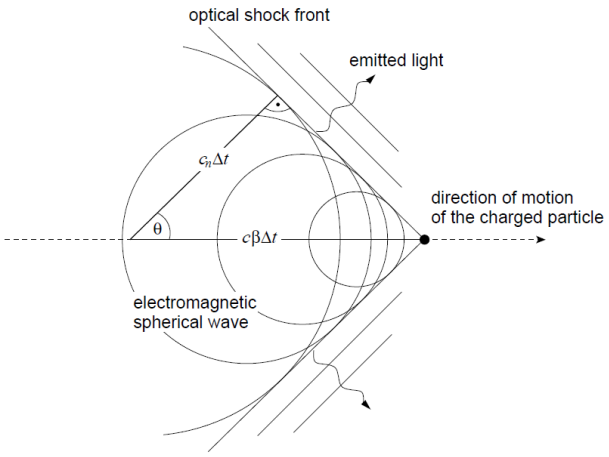

Fig. 2.4: Geometric illustration of the Cherenkov angle for a particle traveling through the atmosphere with velocity $c\beta$ [2].

where n the index of refraction of the dielectric medium and $\beta = v/c$, with c the speed of light in vacuum and v the velocity of the particle. In the Earth's atmosphere n varies height dependent and becomes larger for smaller distances to the ground. That causes the Cherenkov angle θ to become larger for lower altitudes as well. θ moves within in a range of about 1° [12, 7].

2.2 Imaging Atmosphere Cherenkov Telescope

An imaging atmosphere Cherenkov telescope (IACT) is used to track EAS by imaging the emitted Cherenkov radiation. By comparing the images with data generated by Monte Carlo simulations the properties of the primary particle can be determined.
An IACT consists of three main components, namely a reflector, a camera and an electronic system counting the triggered pulses. The underlying principle is shown in Fig. 2.5: If the detector is located somewhere in the Cherenkov light core, the incoming Cherenkov radiation is collected by the reflector and focused onto a pixelized camera. The camera converts the light pulses into electrical signals which are triggered and analyzed afterwards [14].
There are several advantages offered by the utilization of an IACT. For example, due to the Cherenkov light of an EAS arriving in a short period of time of just a few nanoseconds, the corresponding signal is easily separated from the overall night sky background. Furthermore the height dependence of the Cherenkov angle results in a relation between the height of emission and the image taken by the camera which is shown in Fig. 2.5. Cherenkov photons which originate at the beginning of an EAS are emitted in a smaller angle θ while photons emitted at the end of an EAS display larger angles.

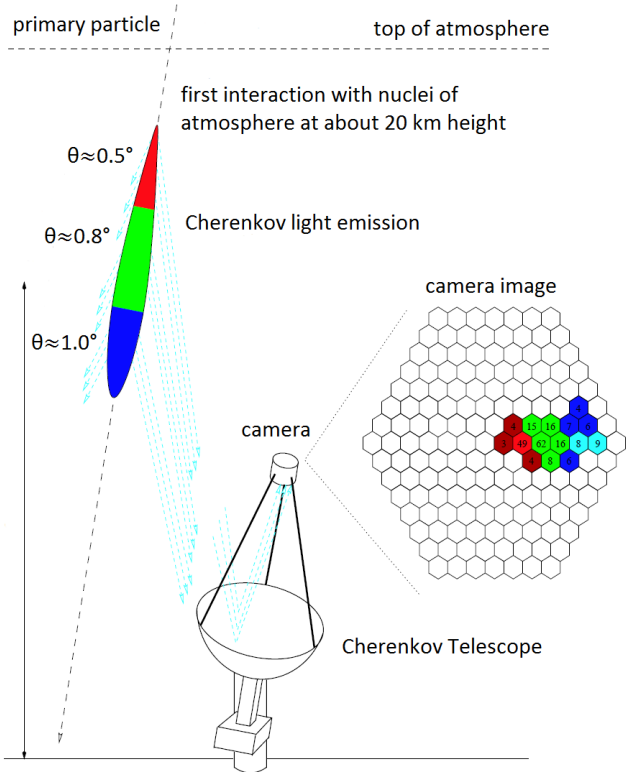

Fig. 2.5: Illustration of an IACT: gamma-ray induces an EAS which emits Cherenkov light in a height dependent angle. Reflector collects and focuses the Cherenkov radiation onto a camera which triggers the signals. Adapted from [15].

Thus photons from the upper part are located nearby the assumed source position in the camera while photons produced at lower altitudes are detected at larger distances from the assumed source position. Together with information about the arrival time of the photons, this allows for space and time resolved pictures of the EAS, an advantage that can be used to distinguish between gamma- and hadron-induced shower events.
The above described differences of both shower-types for example result in differences of the lateral and the angular distribution. Another characteristic for hadronic showers is given due to their muonic part and its relatively large lifetime. Since penetrating particles such as muons travel through the atmosphere faster than the corresponding Cherenkov light, the time spread function becomes larger for hadron-induced EASs than for gamma-induced ones without a muonic component. Those properties can be used to sort out the unwanted background of hadron-induced EASs [12, 2].

2.2.1 Shower characterization

In order to analyze EASs, their images must become parameterized. The most common set of parameters are the “Hillas parameters” [16] that are based on the fact, that most gamma-induced EASs yield an elliptical shaped image. Fig. 2.6 shows some of those parameters illustrated for a source located at the center of the camera. Some of these standard parameters - extended from the original parameter set - are:

- **Size:** Number of all Cherenkov photons in the image
- **Center of gravity (COG):** x- and y-coordinates of weighted center of the ellipse
- **DIST:** Angular distance of COG towards the expected source position in the camera
- **Length/Width:** Standard deviation along the major/minor axis of the ellipse
- **Delta (δ):** Angle between the major axis and the x-axis of the camera
- **Alpha (α):** Angle between the major axis and the vector between assumed source position and COG
- **Distance of closest approach (DCA):** Distance between assumed source position and the extended major axis of the ellipse
- **DISP:** Angular distance of COG to reconstructed source position
- **Theta (Θ):** Angular distance between reconstructed and assumed source position

Further parameters describing potential asymmetries of the shower events or considering time relevant information are:

- **Asym:** Distance between center of ellipse and highest pixel
- **M3Long/M3Trans:** Third moment of the distribution along major/minor axis
- **SlopeLong/SlopeTrans:** Slope of the arrival time along major/minor axis
- **(Weighted) TimeSpread:** (Weighted) standard deviation of the arrival time

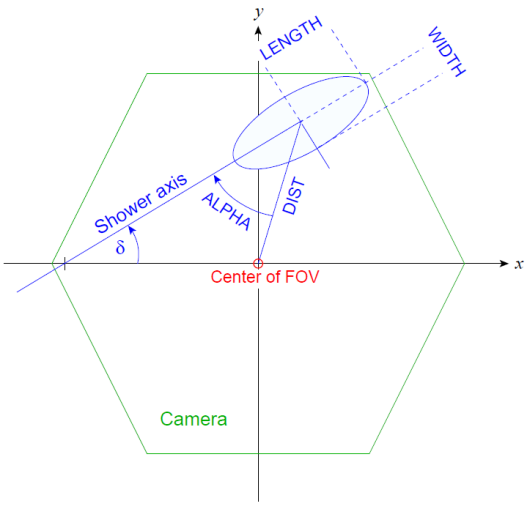

Fig. 2.6: Some shower parameters for a source located at the camera center [2].

- **(Weighted) SlopeSpread:** (Weighted) spread of the arrival time around the slope along the major axis

Those and some others quality parameters are the basis for sorting out events not coming from the observed source, distinguishing between gamma- and hadron-induced EASs and analyzing the properties of the incoming primary particle.

2.2.2 Monte Carlo simulation of extended air showers

In order to determine reliable cut parameters and draw conclusions about the incoming gamma-ray, Monte Carlo data needs to be generated. For this purpose the program **CORSIKA** (**CO**smic **R**ay **SI**mulations for **KA**scades) is the most common one. It tracks an incoming particle traveling through the atmosphere and simulates its interactions with the Earth's atmospheric nuclei or the its decays. These result in further particles that are tracked too, thus whole EASs are simulated [17].
There are several adjustable options for the shower simulation, such as the energy and type of the incoming particle, properties of the Earth's magnetic field or the height of the first interaction. Of special interest for the IACT analysis is the option of simulating the Cherenkov radiation created by the EAS.
The results of a CORSIKA-run can be fed to a program simulating the IACT reflector, camera and its data acquisition. The result is a simulated camera image of an event created by a primary particle with known properties.

3 First G-APD Cherenkov Telescope

The First G-APD Cherenkov Telescope (FACT) is the first IACT using Geiger-mode avalanche photodiodes (G-APDs) as photo sensors. In 2011 it was built on the Canary Island of La Palma at about 2200 m above sea level with the aim to prove the reliability of solid state photon counters in Cherenkov astronomy. Apart from that, FACT was put up for long-term monitoring of some bright active galactic nuclei in the TeV range [18].

3.1 Solid state photomultipliers

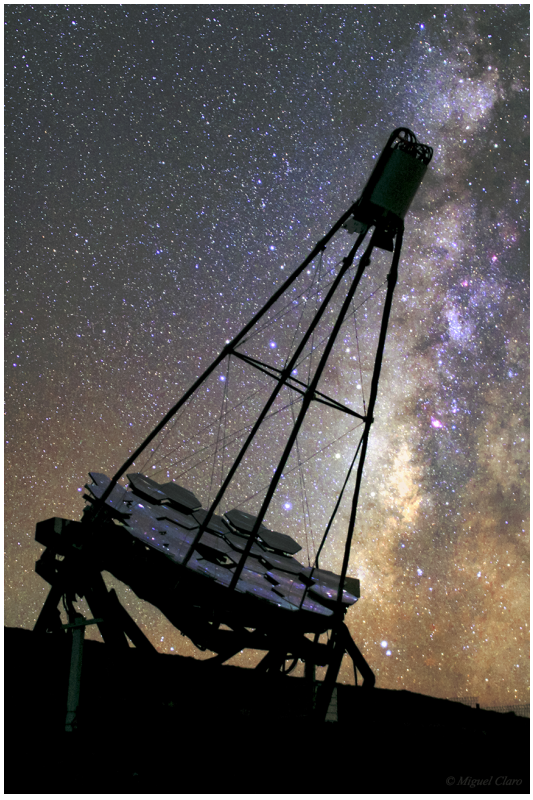

Fig. 3.1: FACT during night, photography taken from [19].

For all IACTs built until 2011 photomultiplier tubes have been used for the detection of the Cherenkov light. This was justified by a good photon detection efficiency of 20 - 30% in the needed area of wavelength and a high intrinsic amplification in the order of 10^5 up to 10^7. But they also reveal some drawbacks like limitations for the further increase of the photo detection efficiency, a high vulnerability to high light levels or a sensitivity to magnetic fields. Especially the vulnerability to a large quantity of photons limits the efficiency due to the inability for observations in bright moonlit nights [15].

Robust semiconductor devices can overcome those problems, since G-APDs are able to keep the high intrinsic amplification while featuring the potential for an even higher photon detection efficiency. Furthermore they are insensitive to magnetic fields and almost do not suffer from operating under unfavorable weather

conditions. This extends the duty cycle and potential observation times heavily [20]. Thus 1440 photo sensors, each consisting of 3600 single Geiger-mode avalanche photo cells and, have been applied in the FACT camera [18].

3.2 Reflector design

The reflector spans a total reflective surface of 9.51 m^2 which is covered by 30 hexagonal shaped mirrors [21]. The fragmentation into several individual mirrors is founded in a cheaper price and an improved flexibility for the reflector design.
There are basically two designs of interest, namely the Davies Cotton design and the parabolic design. In the Davies Cotton mirror arrangement all mirrors have the same focal length and are placed at their focal distances to the focal point. In order to get a spot as bright as possible, the mirrors are orientated towards a point at twice the focal length. This leads to an image with a minimal point spread function and thus an optimized spatial resolution [22].
A paraboloid multi mirror reflector design places the mirrors on a paraboloid. Thus every photon collected by the reflector has to travel the same distance to the focal point. That means a superior time resolution compared to the Davies Cotton design. Both setups offer some advantages and drawbacks for the usage in the FACT aperture. Since the disadvantage of an inferior temporal resolution seemed to be negligible, the original mirror setup of FACT was chosen to be built in Davies Cotton design in order to benefit from the superior spatial resolution. But measurements of the overall temporal resolution of FACT, including all electronic read out components, resolved it to be in the range of about 0.6 ns, which is right in the order of the time spread caused by the Davies Cotton design. Thus the choice of the Davies Cotton design seemed to have significant impact on the temporal resolution. Therefore it was reasonable to hope that a hybrid design combining the advantages of the Davies Cotton design and a parabolic alignment decreases the overall time spread of incoming photons [21].
Indeed this is the fact, so that the reflector is now designed in a hybrid arrangement. It can be described by:

$$G_{HY}(\alpha) = \alpha G_{DC} + (1 - \alpha) G_{PA} \tag{3.1}$$

G_{HY}, G_{DC} and G_{PA} are parameters describing the geometry of the hybrid design, the Davies Cotton design and the parabolic alignment. The parameter α, characterizing the level of adjustment, is chosen to be 0.52 for the actual mirror configuration [21].

3.3 Data analysis

The data analysis of FACT is implemented on the ROOT based "**M**odular **A**nalysis and **R**econstruction **S**oftware - **Che**renkov **Obs**ervation **ed**ition" (**MARS CheObs ed.**) and subdivided in several steps. The most important include [23, 24]:

- **CALLISTO** (**CAL**ibrate **LI**ght **S**ignals and **T**ime **O**ffsets):
  Calculates calibration constants for background suppression and bad-pixel treatment by using pedestal and calibration runs. These constants are applied to raw data thus resulting in a calibrated image.

- **STAR** (**ST**andard **A**nalysis and **R**econstruction):
  Performs an image cleaning only survived by pixels with a minimum amount of registered pixels forming an island. Furthermore the time difference between two neighboring pixels must not come below a certain level. The parametrization of the shower event is applied afterwards.

- **GANYMED** (**G**ammas **A**re **N**ow **Y**our **M**ost **E**xciting **D**iscovery):
  Applies cuts in order to identify events most likely induced by gamma-rays coming from the observed source.

- **SPONDE** (**SP**ectrum **ON DE**mand):
  Compares the image parameters of an event with Monte-Carlo simulated data and draws hereby conclusions about the primary particle energy.

- **CERES** (**C**amera **E**lectronics and **RE**flector **S**imulation):
  Simulates the feedback of the camera for a Monte-Carlo simulated event.

Each program can be used by itself if the corresponding input-files are available. This thesis will deal with the STAR-program.

4 Image correction

For the analysis of the shower properties presented above, it is necessary to consider some distorting effects such as the influence of the Earth's magnetic field on the development of the EAS or optical aberrations due to the reflector design. The last effect and a corresponding correction method have been recently investigated and presented in the bachelor thesis "Development of a new image correction method for the First G-APD Cherenkov Telescope" [25].
This thesis will deal with the application of the presented correction method and research the improvement of the corrected data.

4.1 Optical aberration for FACT design

The reflector design of FACT leads to several optical aberration effects. The lack of consideration of field curvature by the plane camera and the spherical aberration causing a different focus point for rays located near the symmetry axis than for those further away would be two examples for such effects. Therefore it became a topic of interest to characterize the impact of those optical aberration effects on the images taken by FACT in order to adjust them. This has been done by simulating and comparing the images of a photon event from a point-like source given by the actual reflector design of FACT and this of a perfect, plane mirror [25].
The deviation of the COG in radial and azimuthal direction has been calculated for

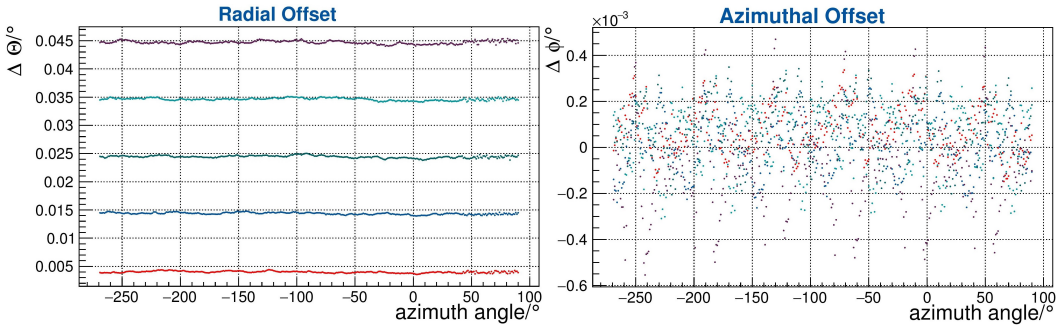

Fig. 4.1: Left: Radial(left) and azimuthal(right) deviation for five different tilt angles and 360 azimuth angles each. Radial offset is almost independent of the azimuth angles and increase for higher tilt angles. Azimuthal deviation seems to be statistically distributed and is about one order of magnitude smaller than the radial one. Adapted from [25].

the five tilt angles 0.2°, 0.7°, 1.2°, 1.7° and 2.2° and respectively each azimuthal

angle between $0°$ and $360°$ in steps of one degree. The deviation in azimuthal direction (see Fig. 4.1, left) seems to be caused by statistical effects. In contrast the radial offset (see Fig. 4.1, right) is almost constant for all azimuth angles and about one order of magnitude larger than for a Davies Cotton arranged mirror [25]. Comparing the azimuthal deviation to the one in radial direction, it becomes obvious that the azimuthal offset can be neglected since it is one order of magnitude lower than the radial one. Thus it would not have a remarkable impact on the total offset given by

$$\Delta = \sqrt{\Delta\phi^2 + \Delta\Theta^2} \tag{4.1}$$

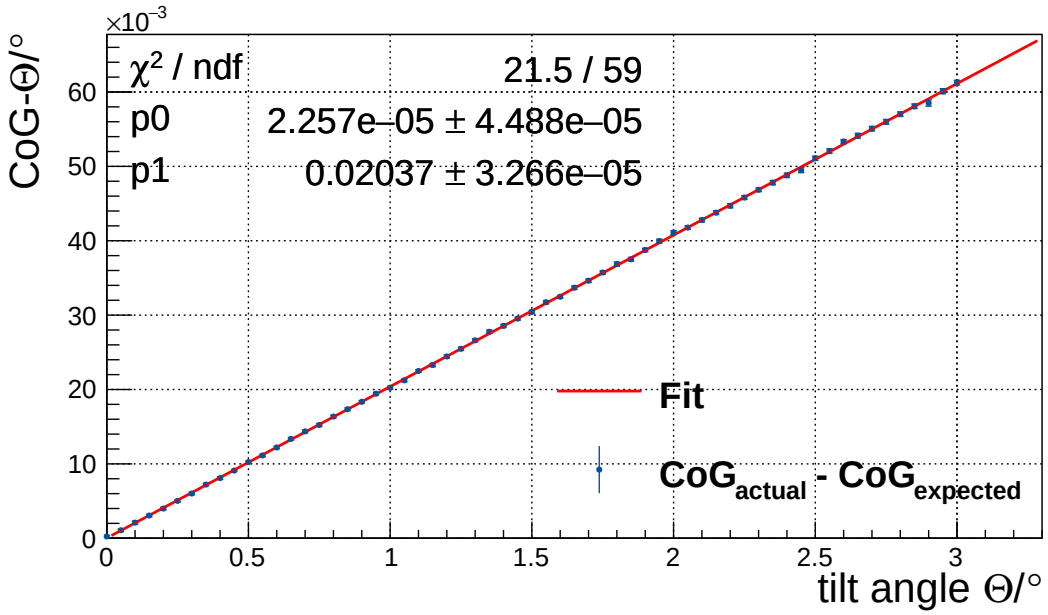

Fig. 4.2: Averaged total deviation against tilt angle θ. A linear fit reveals a linear relation between the total deviation and the tilt angle with a slope of about 0.02. The offset can be neglected since it is - within its error - compatible with $0°$ [25].

performed for tilt angles between $0°$ and $3°$, each for angles from 0 - $360°$ in one degree steps. The resulting values for the COG were averaged, subtracted from the expected COG and the difference plotted versus the expected COG (see Fig. 4.2). A linear fit reveals that due to optical aberrations the COG has been shifted by the fraction $\eta = 0.02$ towards higher distances from the camera center [25].

4.2 Correction method

This distortion can be suppressed by correcting the observed data by the factor $f = 1/(1+\eta) \approx 0.980392$. Therefore after the image cleaning has been done, the center of each hexagonal pixel needs to be shifted by that factor towards the camera center. Afterwards the image analysis can be performed in the familiar way.

5 Implementation of correction method

The correction method described in the section above needs to be implemented in the current analysis software MARS. This is done in the STAR-program, where image cleaning and the parametrization of the shower are executed. During this process, the “MHillasCalc.cc”-function is invoked, that most importantly uses the programs “MHillas.cc”, “MHillasExt.cc” and “MHillasSrc.cc”. Further programs invoked by “MHillasCalc.cc” are not impacted by the image correction and thus do not need to be investigated. Due to the “MHillasSrc.cc”-program working with the corrected output from “MHillas.cc” there is no need for any corrections in this part of the program itself. The most important part of the corrected source code can be found in the appendix (see Listings 7.1 and 7.2). The whole MARS software is freely available at *https://www.fact-project.org/svn/trunk/Mars* for a more detailed look.
In the following paragraphs, the implementation of the correction method for “MHillas.cc” and “MHillasExt.cc” is discussed and the impact on the output files investigated. For this purpose Monte Carlo data has been used in which the assumed source position is located at the camera center. Since the impact of the correction method can be well predicted for both program parts they will be used to prove the correct implementation.

5.1 MHillas.cc

The correction needs to be implemented in the function MHillas::Calc(). Therefore the correction factor fAberration is used, which corrects the positions of the pixels each time they are used (see Listings 7.1). The output parameters are the calculated length, width, delta, size and the x- and y-coordinates of the COG of the shower image. The influences of the correction method are almost obvious and can easily be checked by executing the calculation for given shower events with and without the correction factor and comparing the results afterwards. This yields the following corrections:

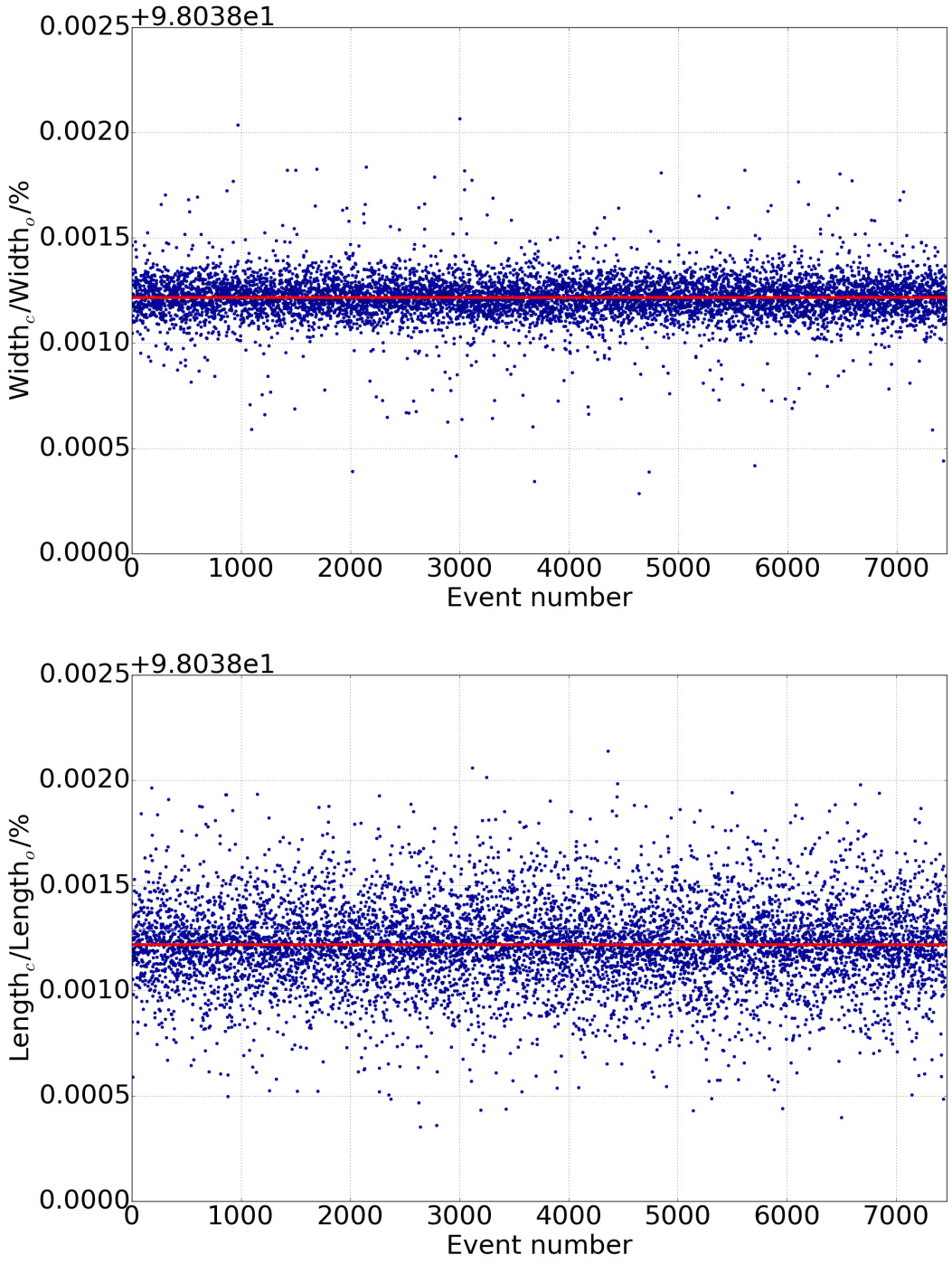

Fig. 5.1: Relative change of width (upper graph, 7458 events) and length (lower graph, 7464 events) for each considered event. The red lines mark the average changes, given by: $\overline{\text{width}_c/\text{width}_o} = 0.980392 \pm 0.000001$ and $\overline{\text{length}_c/\text{length}_o} = 0.980392 \pm 0.000002$.

- **Length, Width:**
  Since both length and width represent the standard deviation along the major/minor axis of the ellipse the correction factor f should contribute directly to a change of the initial parameter by decreasing it by f. Fig. 5.1 verifies this correlation since the average relative change of width is given by

$\overline{\text{width}_c/\text{width}_o} = 0.980392 \pm 0.000001$. Events with an initial or corrected width-value of $0°$ are sorted out in order to determine the mean correctly. An outlier with a very small calculated width ($4.1 \cdot 10^{-6}$ °) is not considered, because the relative change is particularly large due to numerical inaccuracies. The same study yields an overall relative change in length of $\overline{\text{length}_c/\text{length}_o} = 0.980392 \pm 0.000002$. The fluctuations shown in Fig. 5.1 result from numerical inaccuracies and do not need to be minded since they are about three orders of magnitudes smaller than the intended relative change.

- **Delta(δ):**
  δ should not change since the shower is just shifted towards the camera center without any torsion, easily understandable by applying the intercept theorem. Indeed the average correction is given by $\overline{\delta_c/\delta_o} = 0.999999 \pm 0.000003$ (see appendix, Fig. 7.2). Since δ attains values near $0°$ for some shower images, the relatively deviation becomes relative large for some events.

- **Size:**
  Since the total sum of measured photons is not impacted in any way, the correction method has no impact on this parameter.

- **COG:**
  Both coordinates are given by the means of the used pixels weighted with the corresponding number of measured photons. Thus the correction should apply directly on the COG-coordinates by decreasing them by the factor f. That also results in a decreased DIST-value. This is proven in Fig. 7.3 and 7.4 in the appendix. Both, the x- and the y-coordinates of the COG are - despite some fluctuations due to numerical imprecision - decreased by the expected factor.

5.2 MHillasExt.cc

This program delivers further image parameters describing the asymmetry of the image or the arrival time of the photons. The correction is implemented in the same way as in “MHillas.cc”, every time the position of a pixel is requested, its position is shifted towards the camera center (see Listing 7.2).
Since most of the calculated parameters are not as intuitive as the standard Hillas parameters calculated by “MHillas.cc”, it is necessary to take a more detailed look onto the calculations done in “MHillasExt.cc”. These calculations reveal that the corrections of parameters calculated in this part of the analysis are dependent of the correction factor in a simple way, too. For each parameter the expected change is

discussed and compared to the average relative deviation resulting from performing the calculations:

- **Asym:**
  Since the COG and the pixel with the highest amount of registered photons both are shifted by the same factor, the intercept theorem yields a decrease of Asym of the same factor f. The average change of $\overline{\text{Asym}_c/\text{Asym}_o} = 0.9804 \pm 0.0005$ confirms this assumption, although some shower images with small Asym and thus a inaccurate relative change contribute to a slightly divergent overall change (see appendix, Fig. 7.5).

- **M3Long/M3Trans:**
  The third moment along the major and minor axis is normalized and thus the correction should affect M3Long and M3Trans by reducing it by f. Indeed this happens and after eliminating some outliers the overall changes are given by $\overline{\text{M3Long}_c/\text{M3Long}_o} = 0.98039 \pm 0.00003$ and $\overline{\text{M3Trans}_c/\text{M3Trans}_o} = 0.98039 \pm 0.00006$ (see appendix, Fig. 7.6 and 7.7).

- **SlopeLong/SlopeTrans:**
  SlopeLong/SlopeTrans describes the slope of the arrival time along the major/minor axis. The arrival time is not corrected but the coordinates of the pixel along the axis changes. Thus the original SlopeLong/SlopeTrans-values are divided by the correction factor and should undergo a correction by the factor 1.02. The implemented correction method performs that correction properly (see appendix, Fig. 7.8 and 7.9).

- **TimeSpread/TimeSpreadWeighted:**
  No correction is applied to the arrival time and thus there is no change in the (weighted) time spread.

- **SlopeSpread/SlopeSpreadWeighted:**
  The corrections made during the calculation of the (weighted) SlopeSpread cancel each other out, thus there is no correction.

All corrections show - despite some deviations due to numerical inaccuracies - the impact which was expected by investigating the corresponding calculations. That indicates the correct implementation of the correction factor.

6 Impact of correction method

As shown in the section above, the image correction has been applied successfully. Therefore in this chapter the impact on the data analysis is investigated. Especially the resulting changes of α, DCA and Θ^2 are of greater interest since they may provide a potential advance for the overall resolution of FACT.

6.1 Reconstruction of source position

For real observations, the exact source position in the camera is not always known (e.g. due to uncertainties in the tracking or imprecise knowledge of the actual source position). Thus the source position is reconstructed from the shower image. The most common method to reconstruct the source position is the so-called DISP method. It uses the orientation of the major axis of the ellipse as a fixed parameter and assumes the reconstructed source position to be on this line. The point on the major axis, that is closest to the assumed source position (ASP), delivers the best reconstructed position. DIST, DCA and α are known for a Monte Carlo simulated shower and thus the optimal distance DISP_{exp} between COG and the reconstructed source position (RSP) can be calculated for the simulated data by applying the cosine rule. Using that, an algorithm based on the shower parameters aiming to calculate a DISP-value as close as possible to DISP_{exp} can be determined. The parameter Θ is used to quantify the success of the reconstruction as it describes the distance between ASP and RSP.
If FACT aims directly towards the origin of the gamma-ray, the source position in the camera is located at the camera center. In this case α describes the same property as δ. The correction method just shifts the shower towards the source position and α is not affected at all, while DCA and Θ^2 obviously become smaller. It is evident that the correction method affects the resolution for those shower images in a positive way. But there are observation modes in which the object of interest is not located at the camera center, for example for measurements performed in the so-called “wobble-mode”. This observation method is performed in order to determine the background behind the source [26]. In order to prove that the image correction also results in an improved resolution for those kinds of observations, the following investigation deals with such images. Therefore Monte Carlo simulations have been performed with the

source position randomly distributed around the camera center with a distance of 0.6°, the common distance used for images taken in the “wobble-mode” [27].

6.2 Alpha (α)

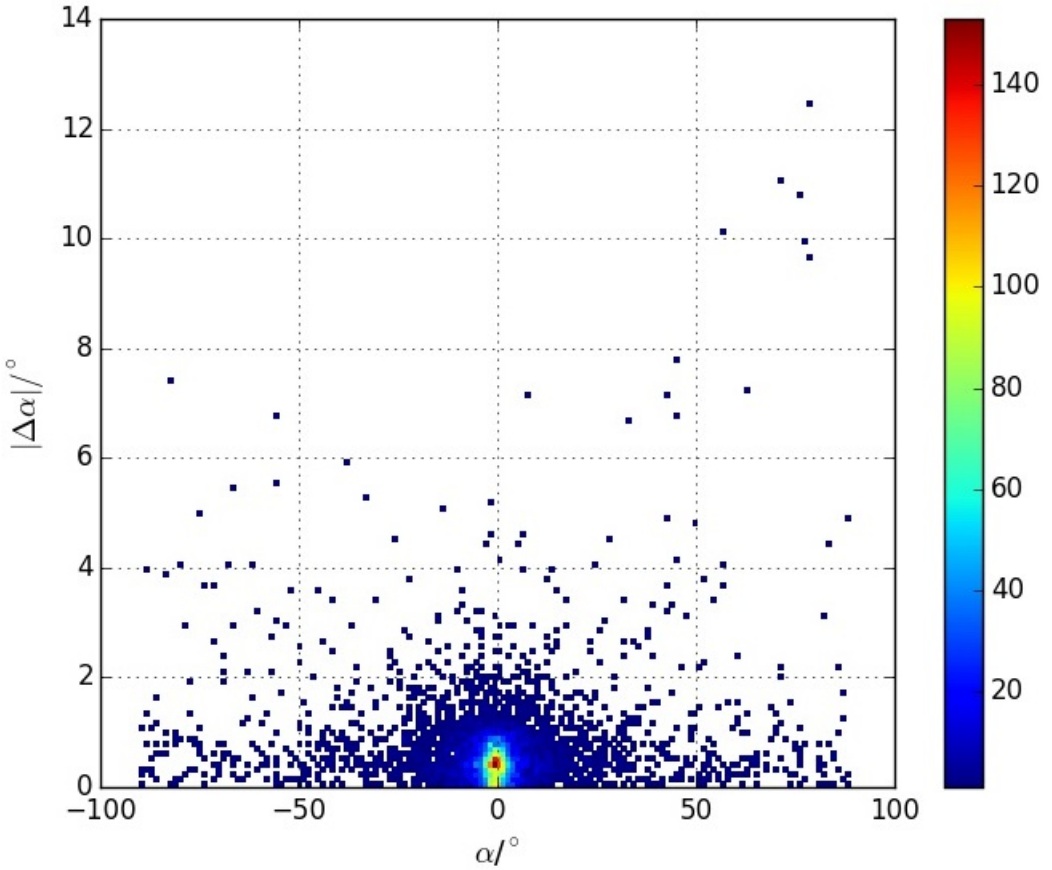

Fig. 6.1: 2D-histogram of the absolute value of $\Delta\alpha$ against the initial α-value, 7622 events. $\overline{|\Delta\alpha|} = 0.59^\circ \pm 0.74^\circ$.

The first parameter to be examined further is α. Since the change of α is randomly distributed around zero (see appendix, Fig. 7.10), it is reasonable to look at the change of the absolute value of α (see Fig. 6.1). The plot includes all 7622 EASs created by the Monte Carlo simulations that resulted in a triggered event in the camera.

A first quantitative evaluation of the impact on α is given by the average absolute change of α, yielding $\overline{|\Delta\alpha|} = 0.59^\circ \pm 0.74^\circ$. The large standard deviation causes the mean of $|\Delta\alpha|$ to be - within its error - compatible with 0°. Nevertheless, Fig. 6.1 indicates, that the mean seems to be in the right order of magnitude while some outliers raise the standard deviation significantly. Better understanding of the change of α may allow to deal with those undesired events.

6.2.1 Delta α(DIST)

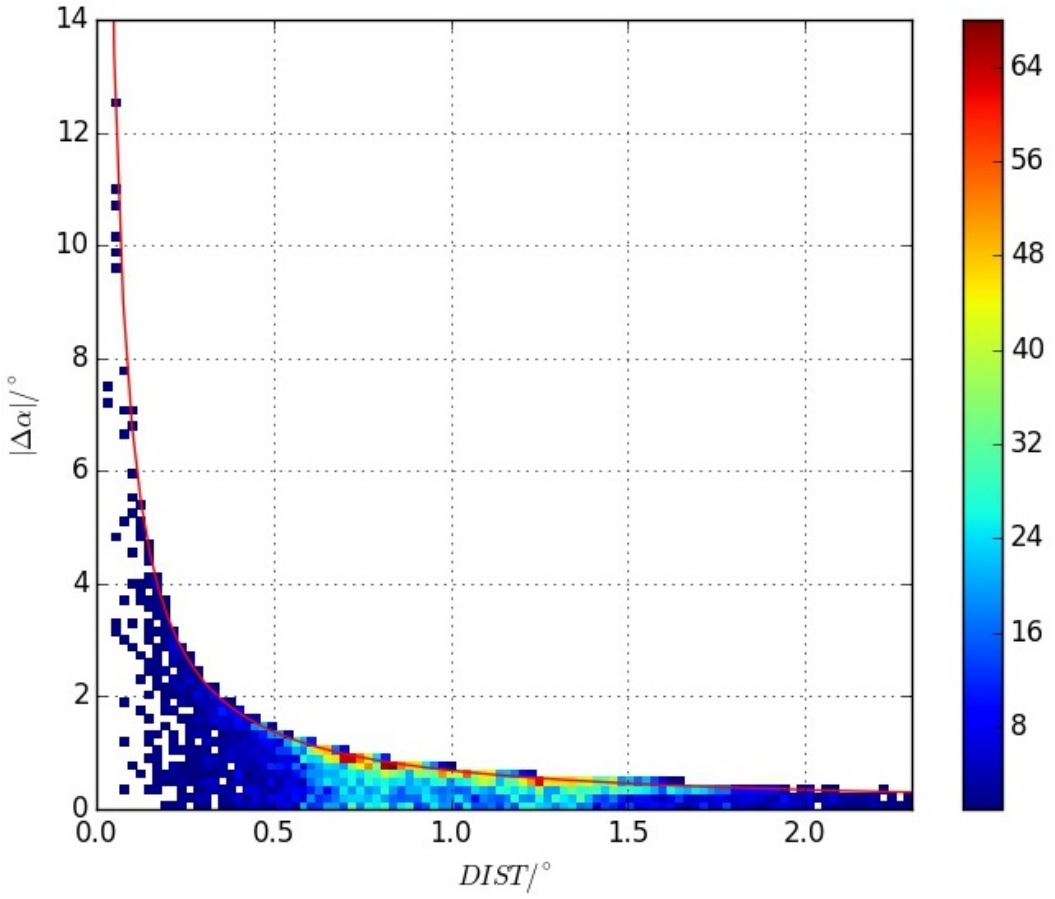

Fig. 6.2: 2D-histogram of the absolute value of $\Delta\alpha$ against DIST, 7622 events. It becomes apparent, that most events are located at distances DIST between 0.5° and 1.5° where the absolute change of α is in a range of about 0.5°-1.5°.

In order to understand the change of α, the absolute value of the change has been plotted against the distance DIST between shower and assumed source position (see Fig. 6.2).

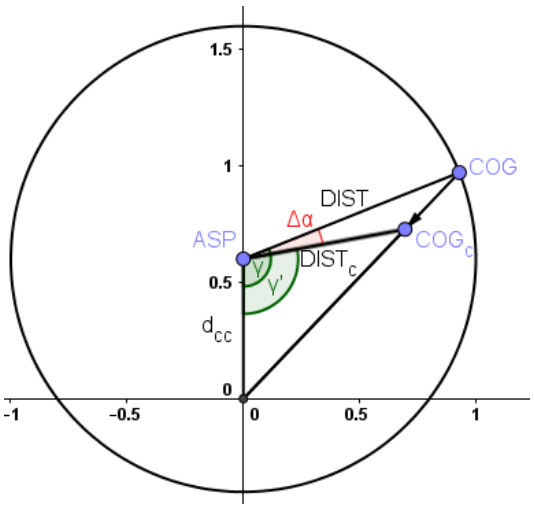

Fig. 6.3: Illustration of the calculation of $\Delta\alpha$.

It becomes obvious, that the biggest changes of α correspond to showers located near the assumed source position. For those showers, α is no convincing parameter anymore since the orientation of the vector between the COG and the assumed source position changes rapidly by small shifts of the COG. A shower may almost point towards the source position but due to the small distance small absolute deviations result in a large angular deviation. Therefore it is generally

considered, that α is no informative parameter for showers located at distances below $0.4°$ from the assumed source position [28]. Those events will not be considered for further research.

In order to understand the structure of Fig. 6.2 the maximal change of α as a function of DIST is determined. Therefore the absolute change of α is calculated for points on a circle with a certain radius DIST around the source position (see Fig. 6.3). Since the orientation of the shower image does not change, the adjustment of γ, the angle between the vectors from the ASP to the camera center respectively to the COG, describe the absolute change of α.

Applying the cosine rule twice and performing some simplifications yields the equation:

$$|\Delta\alpha| = |\gamma' - \gamma| \tag{6.1}$$

$$= \left| \arccos\left(\frac{|\mathrm{COG}_c|^2 - \mathrm{DIST}_c^2 - d_{cc}^2}{-2\ \mathrm{DIST}_c\ d_{cc}} \right) - \gamma \right| \tag{6.2}$$

$$= \left| \arccos\left(\frac{(1-f)d_{cc} + f\mathrm{DIST}\cos(\gamma)}{\sqrt{d_{cc}^2(1-f)^2 + f^2\mathrm{DIST}^2 + 2\ \mathrm{DIST}\ d_{cc}\cos(\gamma)(f-f^2)}} \right) - \gamma \right| \tag{6.3}$$

where d_{cc} the distance from ASP to the camera center.

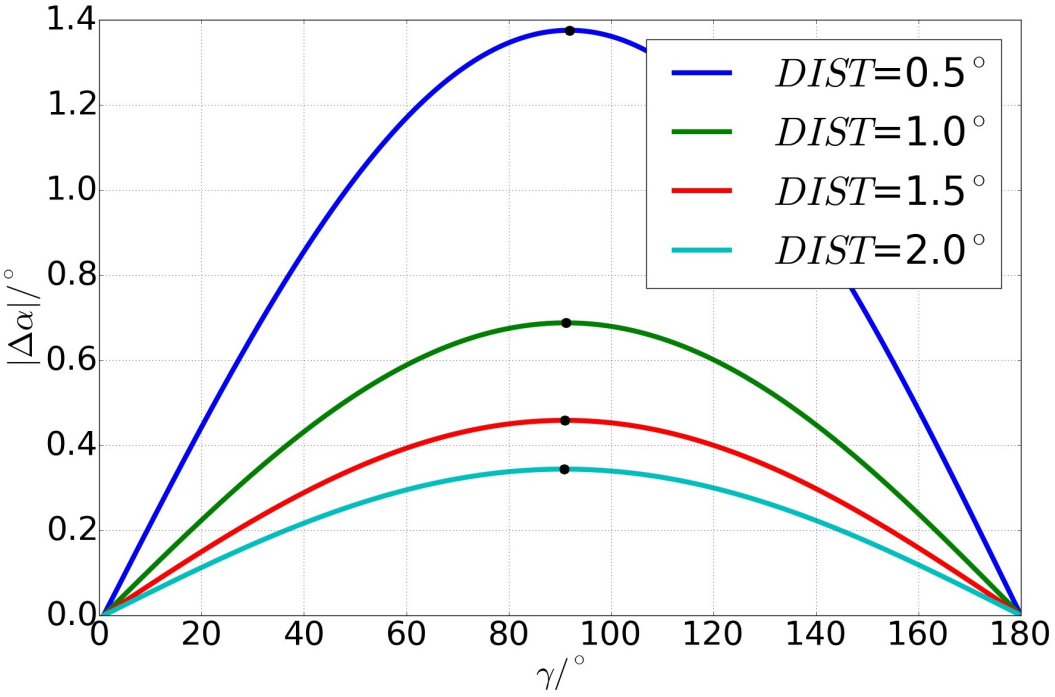

Fig. 6.4: Equation 6.3 plotted against γ for different DIST-values. The maximum of each curve is highlighted. These maximums are located at γ in a range of about 90°.

Fig. 6.4 shows the γ-dependent performance of equation 6.3 for four different DIST-values. Since $|\Delta\alpha|$ reaches its maximum for $\gamma \approx 90°$, it is feasible to use the

estimation $\gamma_{max} = 90°$ and thus maintain the maximal change of α for a given DIST as:

$$|\Delta\alpha|_{max}(\text{DIST}) = \arccos\left(\frac{(1-f)d_{cc}}{\sqrt{d_{cc}^2(1-f)^2 + f^2\text{DIST}^2}}\right) - 90° \tag{6.4}$$

The red line shown in Fig. 6.2 displays this limitation. Despite a few events exceeding the limitation it is valid for almost all considered shower images.

6.2.2 Comparison between corrected and original α

A change of α does not necessarily imply an improved shower orientation, since showers could be turned away from the ASP. Therefore the distribution of α before and after the application of the correction method is investigated. If the width of the distribution is reduced, the showers have been rotated towards the ASP and thus the correction method yields an improved shower orientation.
Fig. 6.5 shows the distribution of alpha with and without correction. Events with DIST-values below $0.4°$ are not considered. The root mean square (RMS) for the original data yields $RMS_o = 14.24°$ against $RMS_c = 14.22°$ for the corrected data. This is a first, but small and almost not evident indication for an improved α-distribution. At least the correction does not worsen the distribution of the shower orientation.

Events with large α often correspond to shower images that are error-prone in

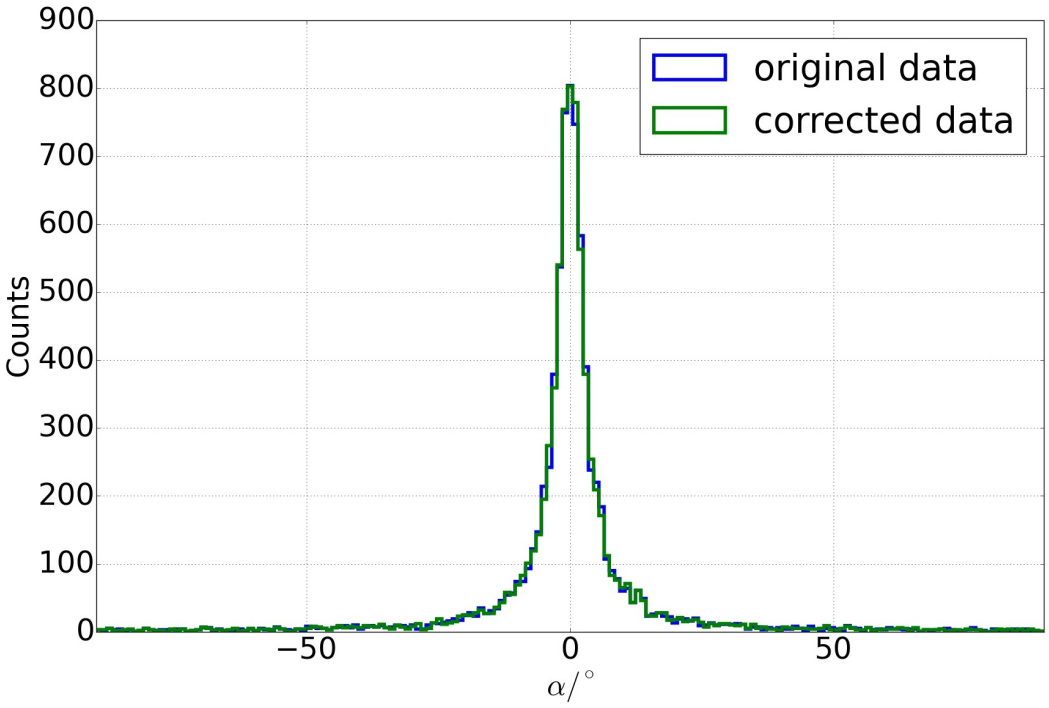

Fig. 6.5: Histogram of α for original and corrected data, 7107 events. $RMS_o = 14.24°$ and $RMS_c = 14.22°$.

the reconstruction of the source position. Those large α-values increase the RMS extremely strong and hence falsify the determination of the improvement of the resolution. Therefore, it is reasonable to neglect the corresponding shower images for the evaluation of $\Delta\alpha$.
Small events using just a small amount of pixels are the most common origin of those increased α-values. These shower images have preferred orientations due to the restricted image resolution and therefore the corresponding major axes cannot point directly towards the ASP. The mean of the number of used pixels of all simulated Monte Carlo data is about 16. By eliminating events which are using less pixels most of those shower images with large $|\alpha|$-values are sorted out.
In addition round shower images, which have no clear orientation, often display randomly large α-values. They are eliminated by cutting all events whose length-to-width-ratio is below 2.0.

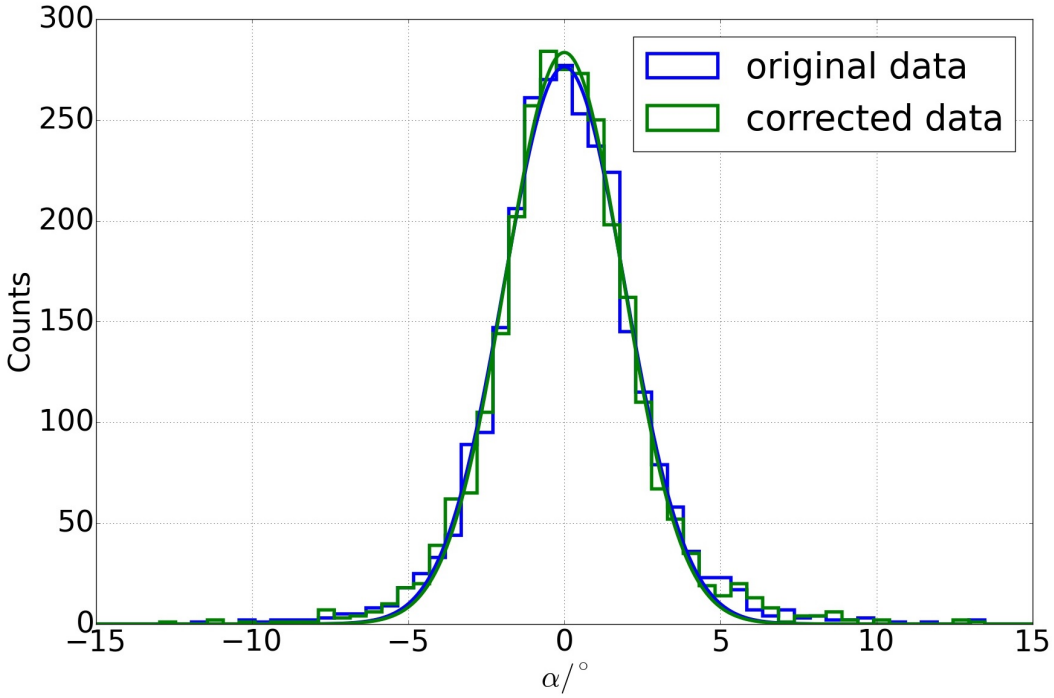

Fig. 6.6: Histogram of α for original and corrected data, 2751 events. A Gaussian function is fitted to each data set yielding the standard deviations $\sigma_c = 1.88° \pm 0.02°$ and $\sigma_o = 1.94° \pm 0.03°$. Thus the corrected data are rotated towards ASP.

After applying those cuts there are 2751 shower images left and as expected it seems that all potentially defective events are eliminated (see Fig. 6.6). Since the distributions show a curve shape similar to a to the y-axis symmetric Gaussian bell, a Gaussian function of the form

$$f(x) = \frac{A}{\sigma\sqrt{2\pi}} \exp\left(-\frac{1}{2}\left(\frac{x}{\sigma}\right)^2\right) \tag{6.5}$$

is fitted to both histograms. The standard deviations σ resulting from both fits are used to evaluate the potential improvement of the correction method on the shower

orientation of sound shower images. The determination of χ^2 is of no interest, since Fig. 6.6 shows, that the fitted functions approximately fit the shape of the data and thus can be used as quantifiers for the width of the distributions.
It is feasible, that the distribution of the corrected data is slimmer than the one of the initial data. This also displays in the standard deviation $\sigma_c = 1.88° \pm 0.02°$ which is smaller than $\sigma_o = 1.94° \pm 0.03°$ for the original data set.
The events set out in Fig. 6.6 are the most solid and reliable data. Thus it is justified to quantify the impact of the correction method by the changes of the corresponding images. The correction yields a reduction of the width of about 3.1%. Since the correction has at least no negative impact on the other data (proven by the slightly reduced RMS) it is demonstrated, that the correction method impacts α in the intended way and turns the shower images towards the ASP.

6.3 Distance of Closest Approach (DCA)

Because DCA describes the lowest possible distance between ASP and RSP, the change of DCA is of further interest. For showers near the assumed source position the large change of α has no strong impact on DCA while a relative small change in α for showers with larger distances becomes relevant. Since the point of closest approach between the major axis and the ASP is associated with the ideal RSP, a decrease of the absolute value of DCA would indicate an by the correction method optimized shower image.

6.3.1 Delta DCA(DIST)

Since the change of DCA is statistically distributed around zero degree (see appendix, Fig. 7.11), the absolute change of DCA is plotted against DIST (see Fig. 6.7).
As expected this parameter shows less dependence on DIST than α. Most showers feature a change of |DCA| which is statistically distributed between 0° and 0.014°. Nevertheless there are some outliers visible. They originate from showers orientated almost perpendicular to the vector between camera center and COG.

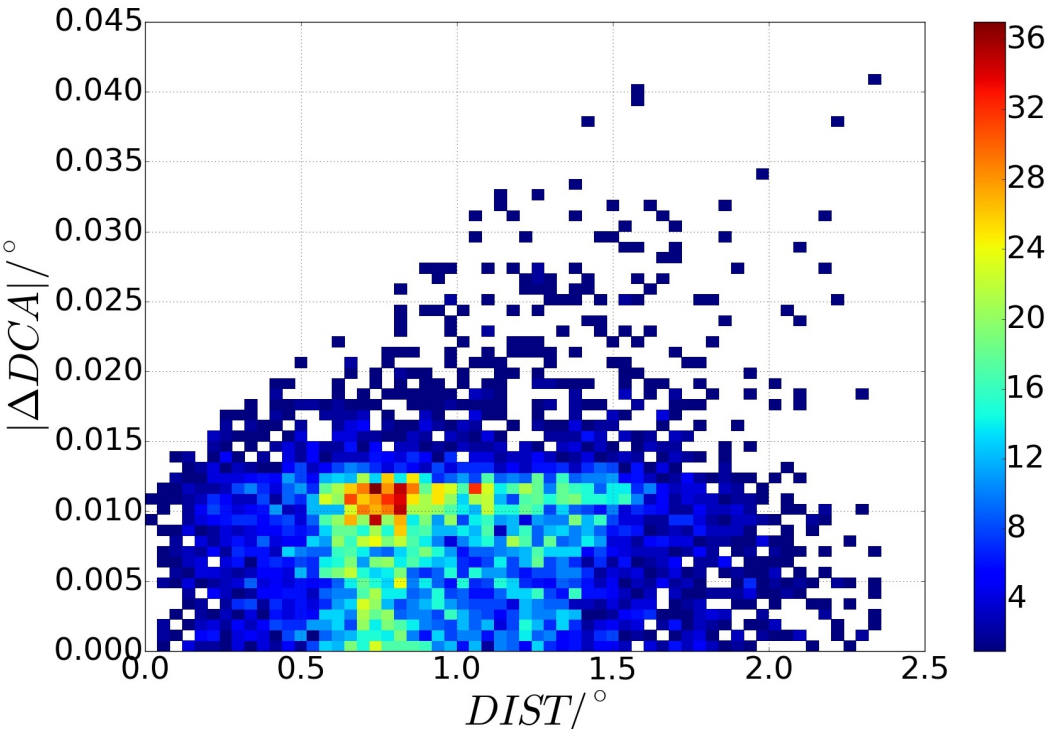

Fig. 6.7: 2D-histogram of absolute value of DCA against DIST, 7622 events. ΔDCA is limited by a linear relation (see eq. 6.6). Accumulation of events for DIST between $0.5 - 1.5°$ and ΔDCA between $0 - 0.012°$.

For those showers the correction has the largest impact on DCA as the shift of the COG directly converts into a change of DCA. Therefore |Δ DCA| is limited by a straight line given by:

$$|\Delta \text{ DCA}|_{max} = (1 - f) \; |\text{COG}| = (1 - f) \;\; (0.6^\circ + \text{DIST}) \tag{6.6}$$

Because the source position in the used Monte Carlo simulations is located $0.6°$ away from the camera center the offset of $0.6°$ is justified. Fig. 6.7 indicates that there might be systematics for the change of DCA. For DIST-values between 0.5° and 1.5° there seems to be an accumulation of events with an absolute change of DCA of about $0.012°$.

6.3.2 Delta DCA(|COG|)

The systematics mentioned above can be better understood by plotting |Δ DCA| against the distance of the COG to the camera center (see Fig. 6.8).

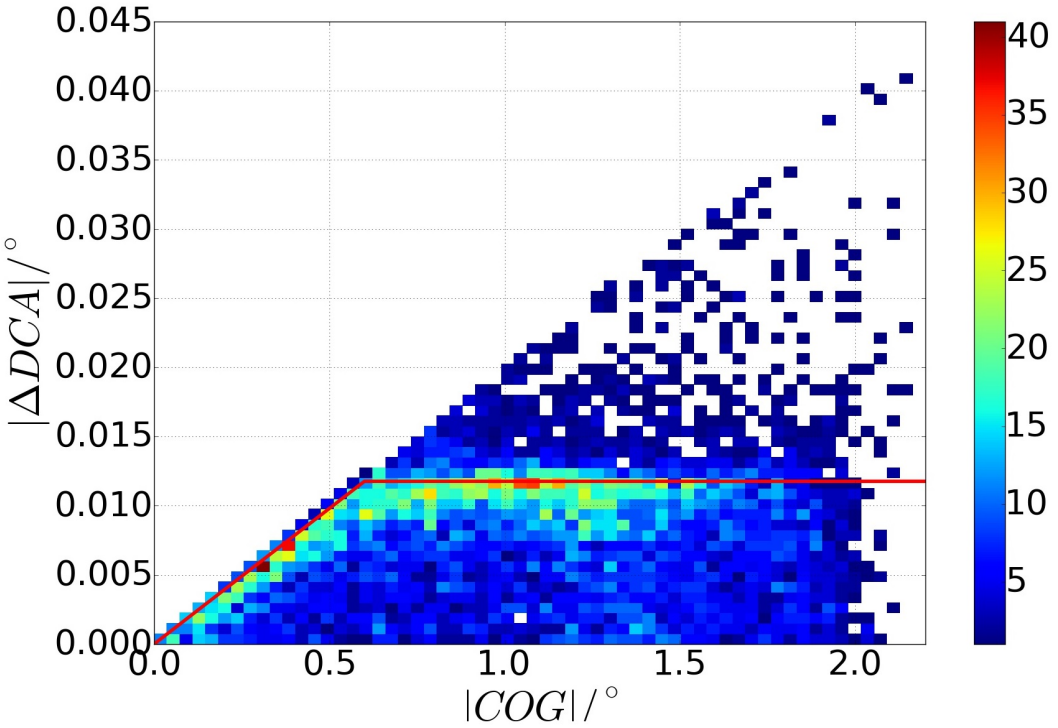

Fig. 6.8: Absolute value of DCA against distance towards camera center, 7622 events. Red line displays upper limit of ΔDCA for events with $\alpha \approx 0°$. Events that does not fit that estimation exceed the limitation.

First of all there is the obvious limitation already stated by equation 6.6. In addition it becomes even more obvious that the preferred absolute change of DCA is at around $0.010-0.012°$. This is founded in the distribution of $|\alpha|$. For most events the shower image points approximately towards the assumed source position and thus they feature small values of α. Out of 7622 simulated events 4934 exhibit an uncorrected α-value below $5°$. Therefore it is feasible to make the rough estimation of $\alpha_o \approx 0°$. For this estimation the initial DCA without correction is $0°$. The new DCA and thus the absolute change of DCA can be calculated by:

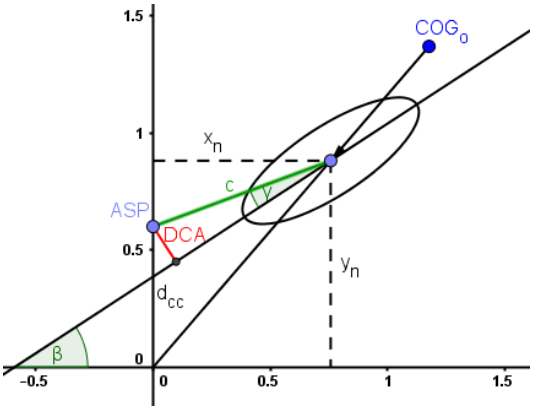

Fig. 6.9: Illustration of estimation of DCA for small α.

$$|\Delta \text{ DCA}| \approx |\sin(\gamma)\ c| \tag{6.7}$$

$$= \left|\sin\left(\beta - \arctan\left(\frac{y_n - d_{cc}}{x_n}\right)\right)\sqrt{x_n^2 + (y_n - d_{cc})^2}\right| \tag{6.8}$$

This is done for 180 orientation angles β uniformly distributed between $0°$ and $180°$ and distances |COG| between $0°$ and $2.2°$. In order to get an upper limit for events

with $\alpha \approx 0°$ the largest absolute DCA for a given |COG| is taken and drawn into the plots in Fig. 6.8.
For distances |COG| below $0.6°$ the estimation exactly coincides with the overall limitation given by equation 6.6. At |COG| $= 0.6°$ there is a sharp knee and the estimations of DCA yield an almost constant value of ΔDCA $\approx 0.0117°$. That value corresponds exactly to a shower orientated perpendicular towards the vector between camera center and ASP. Since any shift towards the assumed source position has no impact on DCA only the shift parallel to that vector contributes to an adjustment of DCA. This shift is given by $(1 - f) \cdot 0.6°$ for the described showers and thus yields immediately ΔDCA $\approx 0.0117°$.
By eliminating all showers with α above $5°$ it becomes obvious that the calculated $|\Delta\text{DCA}|_{max}$ and thus the described shower event constitutes a valid limitation within the underlying estimation (see Fig. 6.8).

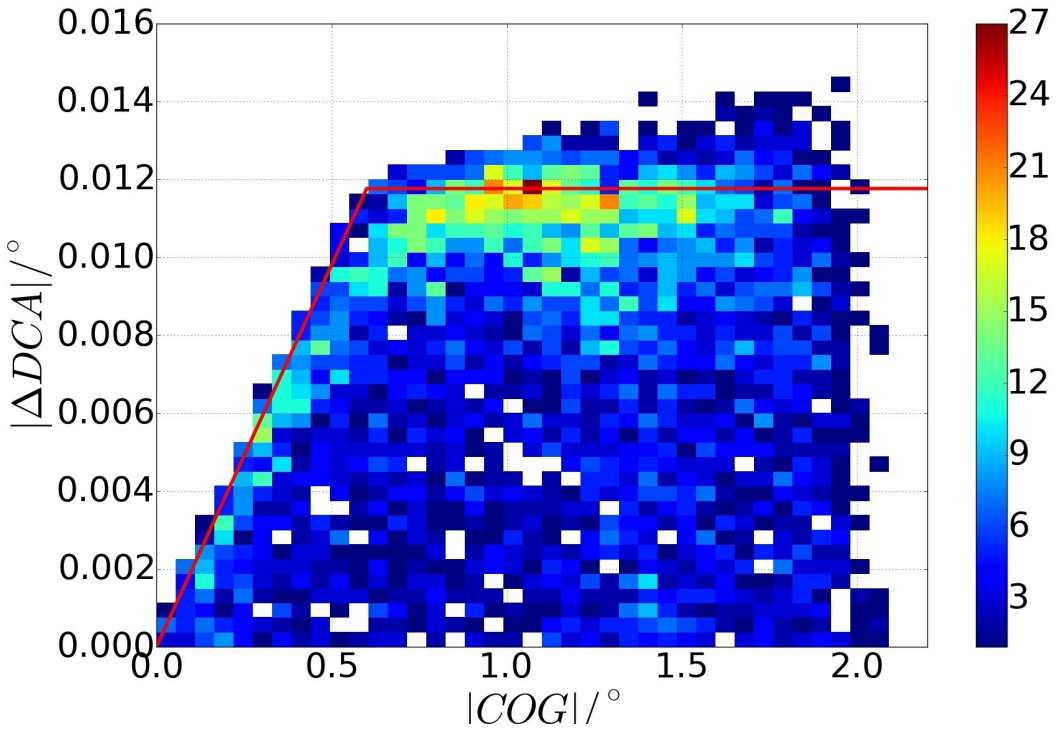

Fig. 6.10: Absolute value of Δ DCA against distance towards camera center, $\alpha < 5°$, 4934 events. Red line displays upper limit of ΔDCA for events with $\alpha \approx 0°$, just small deviations.

6.3.3 Comparison between corrected and original DCA

In order to quantify the change of DCA the distributions of the corrected and the initial data is investigated in the same way it has been done for α. If DCA is impacted in a positive way the distribution should become slimmer for the corrected data resulting in a decreased root mean square.

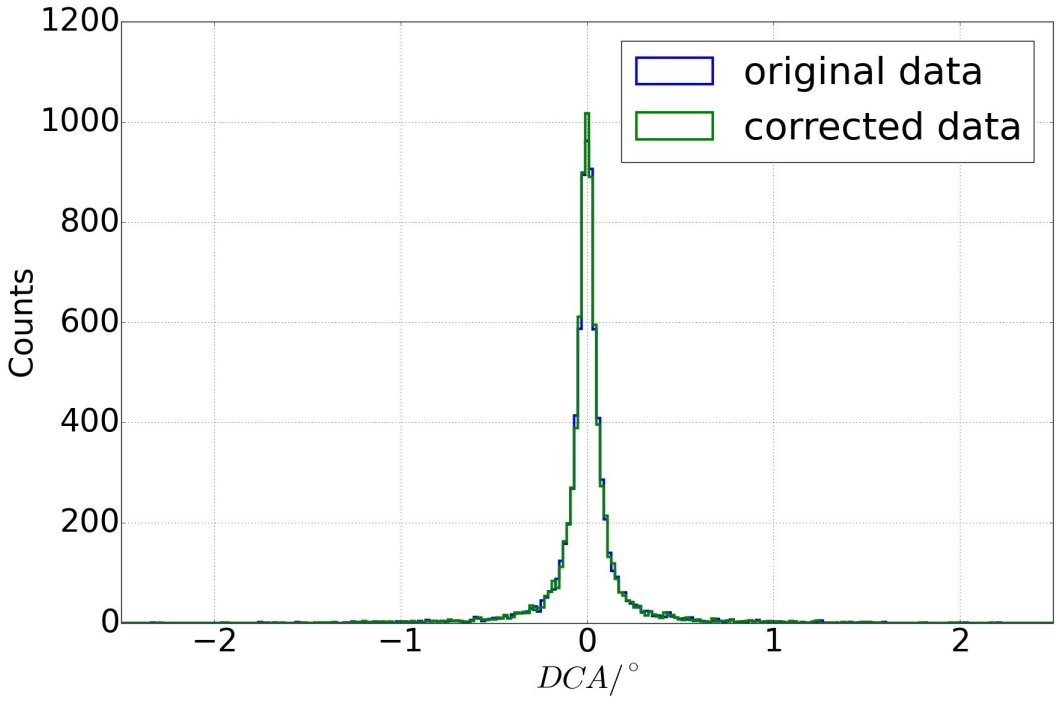

Fig. 6.11: Histogram of original and corrected DCA, 7622 events. $RMS_o \approx 0.216°$ and $RMS_c \approx 0.213°$. The distribution of the corrected data has a smaller width than the one with the original data. The correction method improve DCA.

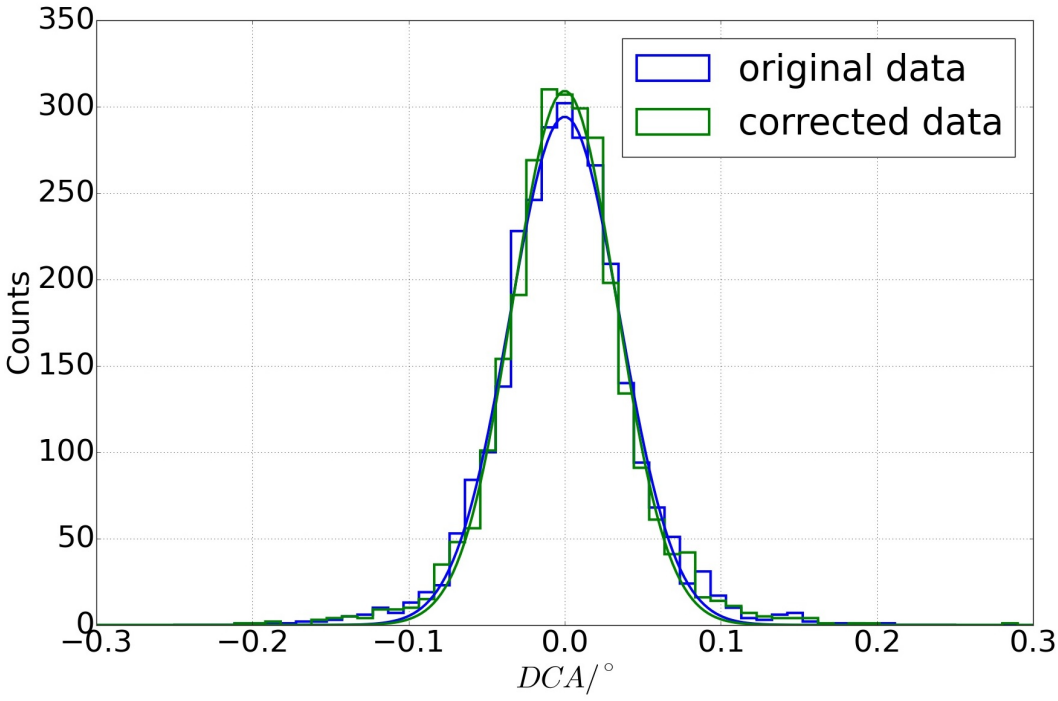

Fig. 6.12: Histogram of original and corrected DCA, several cuts applied, 2751 events. $\sigma_o = 0.035° \pm 0.001°$ and $\sigma_c = 0.033° \pm 0.001°$, correction yield bigger improvement for solid events.

Fig. 6.11 shows the original and corrected data. Obviously the peak has become sharper for the corrected DCA. That affects the root mean square which decreases from $RMS_o \approx 0.216°$ for the original data to $RMS_c \approx 0.213°$ for the corrected DCA. This correlates to a decrease of about 1.4%.
Since this histogram and the root mean square consider all events, including those which might be sorted out during the FACT analysis, the cuts used for the investigation of α are applied too. Thus only meaningful events are treated.
The resulting histogram (see Fig. 6.12) displays distributions with a to the y-axis symmetric Gaussian form. Therefore the same width is quantified in the same way as in section 6.2.2. The standard deviations resulting from the fits are given by $\sigma_o = 0.035° \pm 0.001°$ for the original data and $\sigma_c = 0.033° \pm 0.001°$ for the corrected data. Therefore the correction results in an improvement for the distribution of DCA by reducing its width by about 5.7% for the most solid shower images and about 1.4% if all events are taken into account.

6.4 Theta squared (Θ^2)

The final impact of the image correction method on the overall resolution can be quantified by the parameter Θ^2. Since Θ describes the angular distance between the ASP and the RSP, a reduced mean of Θ^2 would indicate an improvement for the source reconstruction and thus an enhanced resolution of FACT.

6.4.1 DISP algorithm

In order to be able to investigate the change of Θ^2, an algorithm calculating the DISP-value with the least deviation to DISP_{exp} must be developed phenomenologically.
The development of the DISP-calculation is complex because several parameters may have an impact. In order to make that analysis step as simple as possible this thesis will just consider two parameters for determining the reconstructed source position, both introduced in section 2.2.1. Those are the width/length-ratio, shortened as "W/L", and the parameter "SlopeLong", shortened as "slope". Showers pointing directly towards the telescope will result in an approximately round image, thus W/L is about one. Those showers does not need to be shifted in any direction, hence DISP should be $0°$ for those events. In contrast showers with a small W/L-value are associated with a larger shift with respect to the COG.

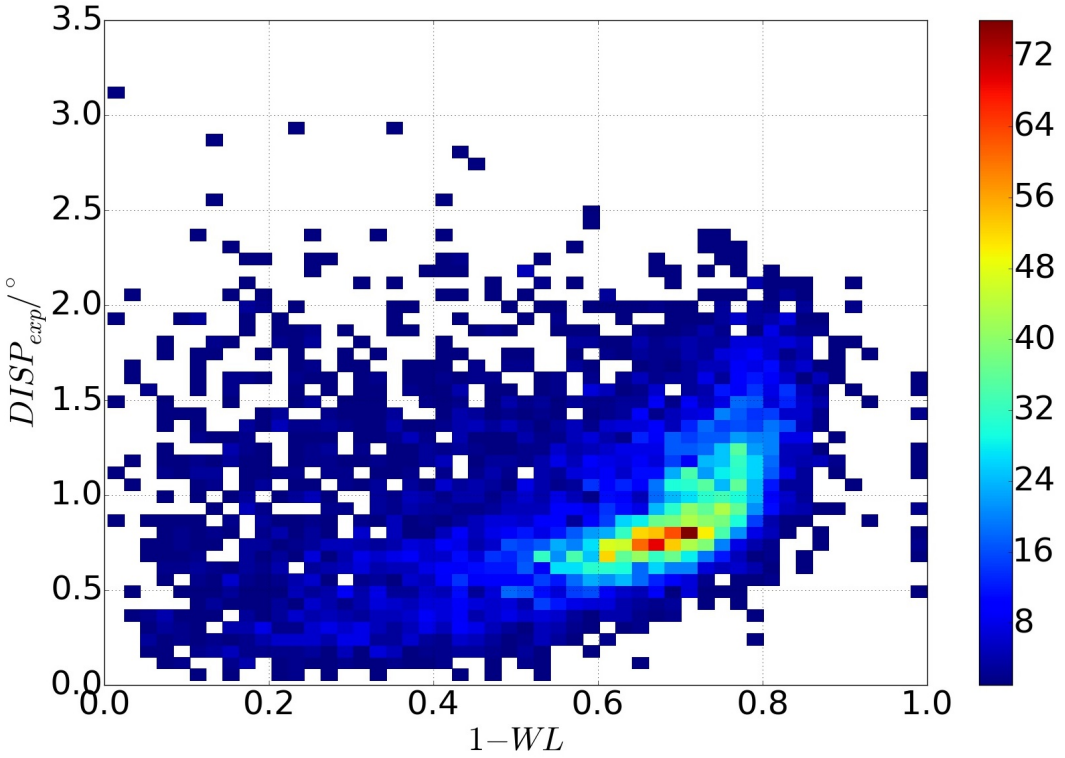

Fig. 6.13: DISP$_{exp}$ plotted against 1−W/L, events with "Leakage1"≠0 sorted out, 6684 events. No clear dependency discernible, thus linear relation estimated.

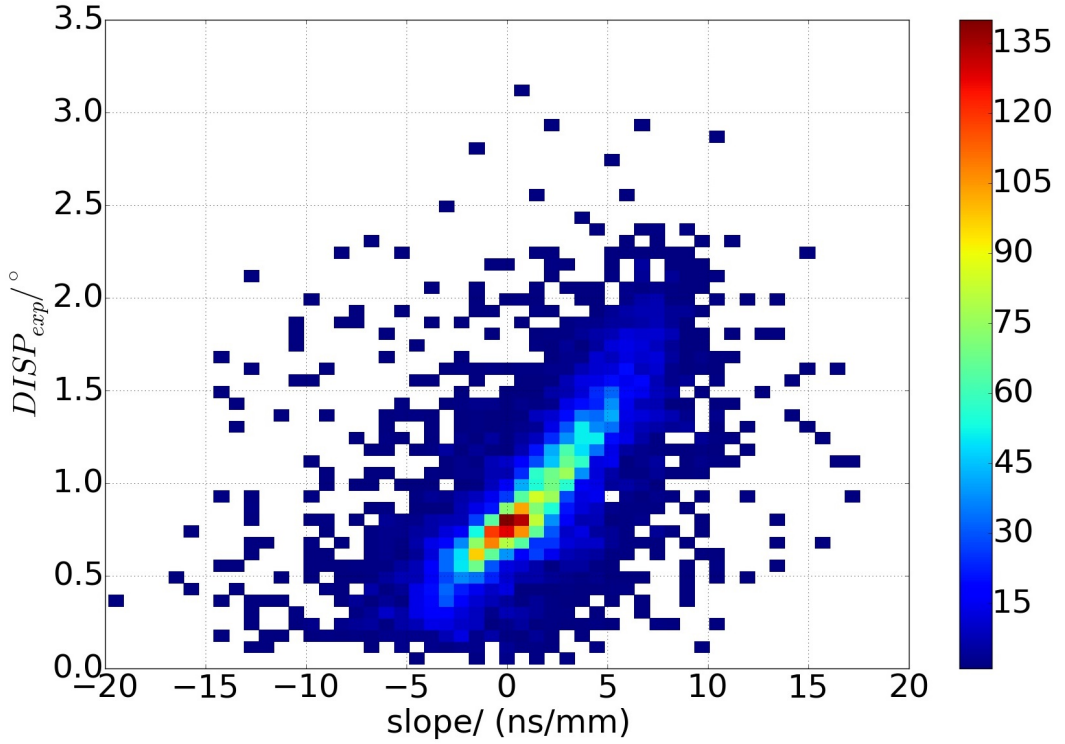

Fig. 6.14: DISP$_{exp}$ plotted against slope, events with "Leakage1"≠0 sorted out, 6684 events. Linear relation visible.

Therefore W/L is the most important parameter for the determination of DISP. Since Fig. 6.13 does not show a clear dependency the influence of W/L on DISP is roughly estimated to be:

$$\text{DISP} \propto (1 - W/L) \tag{6.9}$$

As showers, that have not been detected completely by the telescope, cause distorted width/length-ratios, they are excluded in this thesis. The parameter “Leakage1”, representing the photons in the outer ring camera pixels over the total sum of Cherenkov photons, serves as the cut parameter. All showers that have photons in the outer ring and thus feature non-zero “Leakage1”-values are sorted out.
The impact of the slope-parameter is less intuitive. Nevertheless Fig. 6.14 illustrates a potential relation of the kind of:

$$\text{DISP} \propto a\ (b + slope) \tag{6.10}$$

Both dependencies are combined to:

$$\text{DISP} = (1 - WL)\,(a + b\ slope) \tag{6.11}$$

A non-linear least-square fit is used to fit the function for DISP to the corresponding DISP_{exp}. This fit is performed for the data with and without the correction method applied. The results are shown below in table 6.1.

Tab. 6.1: DISP-fit parameters for function as presented in equation 6.11.

	$(a \pm \sigma_a)/^\circ$	$(b \pm \sigma_b)/\frac{mm}{ns}^\circ$
original data	1.283 ± 0.008	0.111 ± 0.002
corrected data	1.259 ± 0.008	0.108 ± 0.002

6.4.2 Comparison between corrected and original Θ^2

Utilizing the estimated DISP, Θ^2 can be calculated by applying the cosine rule:

$$\Theta^2 = \text{DIST}^2 + \text{DISP}^2 - 2\ \text{DIST}\ \text{DISP}\ \cos(\alpha) \tag{6.12}$$

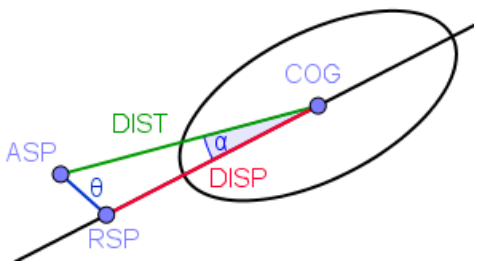

Fig. 6.15: Geometrical illustration of calculation of Θ.

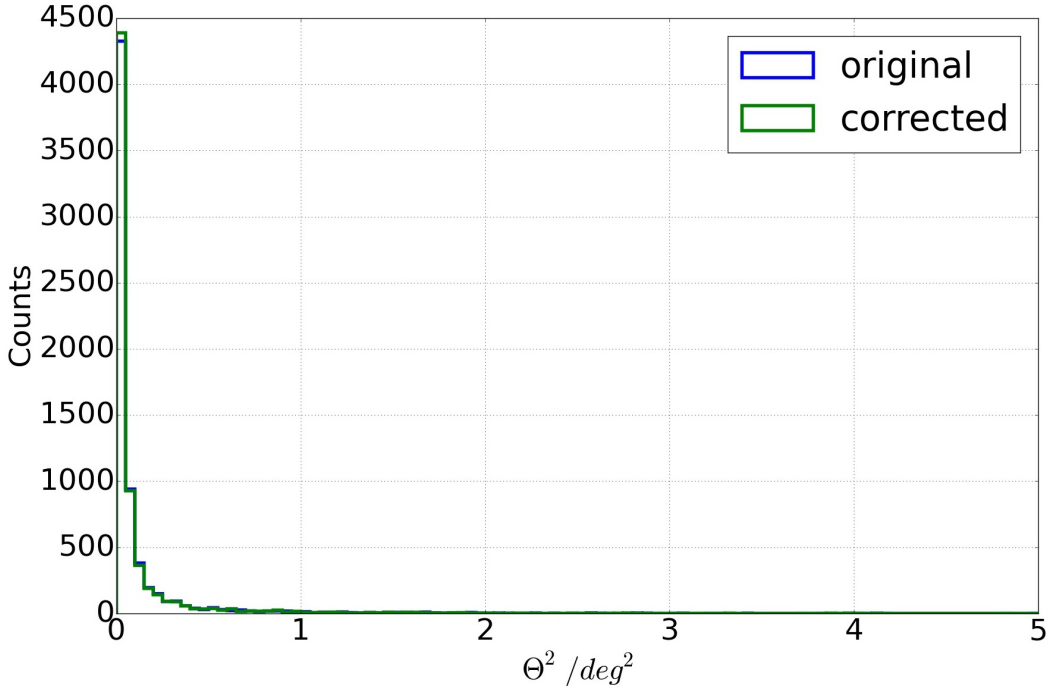

Fig. 6.16: Histogram of Θ^2, just Leakage-cut, 6684 events. $\overline{\Theta^2}_o \approx 0.122\,\mathrm{deg}^2$ and $\overline{\Theta^2}_c \approx 0.117\,\mathrm{deg}^2$.

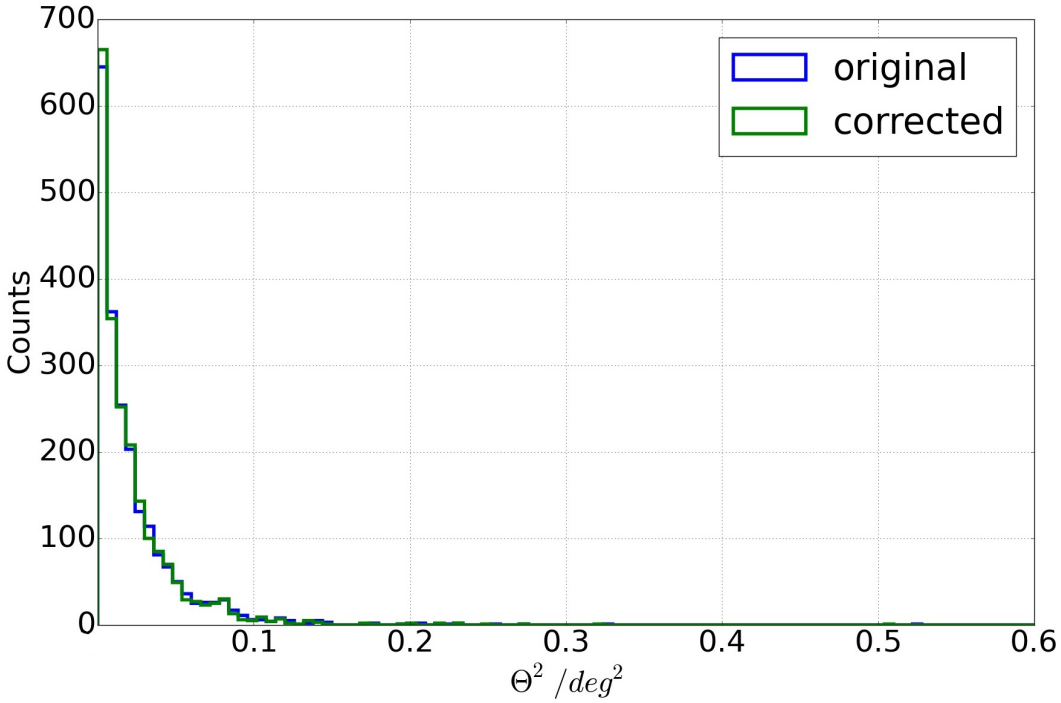

Fig. 6.17: Histogram of Θ^2, solid events, 2130 events. $\overline{\Theta^2}_o \approx 0.0231\,\mathrm{deg}^2$ and $\overline{\Theta^2}_c \approx 0.0223\,\mathrm{deg}^2$.

This is done for the original and the corrected data. A histogram of the resulting Θ^2-values is shown in Fig. 6.16. Despite featuring some large deviations between

ASP and RSP the mean of Θ^2 delivers a decrease from $\overline{\Theta^2}_o \approx 0.122\,\mathrm{deg}^2$ to $\overline{\Theta^2}_c \approx 0.117\,\mathrm{deg}^2$ for the shower image with applied correction method. That corresponds to an average relative improvement of about 4.1%. Obviously the shower reconstruction does not work every time. Even though the distribution strongly flattens for $\Theta^2 > 0.5\,\mathrm{deg}^2$, there are events with a deviation of $|\Theta| > 1\,\mathrm{deg}$ yielding $\Theta^2 > 1\,\mathrm{deg}^2$. Those large deviations contribute strongly to the mean value.
Most of those events feature large $|\alpha|$-values and does not point towards the ASP. They may not represent the impact of the correction method correctly because their shower images are not very informative. Therefore the cuts used for the investigation of α and DCA will be applied in this part too.
This yields the following distribution in Fig. 6.17. As expected the reconstruction of the source position is much better for those events with clear orientation and a large amount of used pixel resulting in an improved validity of the corresponding shower image. The corresponding mean values are given by $\overline{\Theta^2}_o \approx 0.0231\,\mathrm{deg}^2$ for the initial data and $\overline{\Theta^2}_c \approx 0.0223\,\mathrm{deg}^2$ for the corrected data. This means an improvement of about 3.5%. As this is the improvement of Θ^2, the actual correction of the resolution is given by the square root of this value. That yields an overall improvement of the spatial resolution due to the correction method of about 1.87%.
It is important to point out, that the analysis of Θ^2 has just limited validity. The fit parameters for the corrected and the original data may work differently well for the corresponding DISP calculation.

7 Conclusion and outlook

A potential implementation of a new image correction method for the First G-APD Cherenkov Telescope has been shown and its influence on the shower image parameters discussed. It was proven that despite some numerical inaccuracies the correction method has the expected impact on the calculated image parameters and thus the presented implementation is correct. The impact of the correction of the image parameters is given by the factors $1/(1+\eta)$ or $1+\eta$ respectively while it has no influence on the rotation of the shower image.

Furthermore the impact on the reconstruction of the source position and thus the improvement of the spatial resolution was investigated. Therefore the impact of the correction method and the corresponding DIST- and |COG|-dependent behavior of the absolute changes of α and DCA were investigated. The occurring systematics has been discussed and qualitatively explained. α and DCA themselves were compared before and after applying the image correction, revealing that the orientation angles of the most solid shower images are in average corrected towards the assumed source position by 3.1%. For those kind of showers, this leads to an improvement of 5.7% for DCA. Error-prone shower images are corrected as well.

Those corrections result in an overall enhanced sensitivity of the telescope, proven by the decrease of the mean of the distribution of Θ^2 of about 3.5% for such events, meaning an enhanced spatial resolution of about 1.87%.

Although the overall improvement is not exceedingly large, it is one contribution to the removal of distorting effects. Thus the next step should be to integrate the image correction for the entire MARS software. A potential way to do it has been presented in this thesis.

Bibliography

[1]T. K. Gaisser and T. Stanev. „Cosmic Rays“. In: *The European Physical Journal C - Particles and Fields* 15.1 (2000), pp. 150–156 (cit. on p. 1).

[2]Sebastian Caspar Commichau. „Observation of Very High Energy Gamma-Rays from the Galactic Center with the MAGIC Telescope, considering Geomagnetic Field Effects on the Imaging Technique“. PhD thesis. ETH Zurich, 2007 (cit. on pp. 1–3, 5–9).

[3]E. Lorenz and R. Wagner. „Very-high energy gamma-ray astronomy“. In: *The European Physical Journal H* 37.3 (2012), pp. 459–513 (cit. on p. 1).

[4]Johannes Bluemer, Ralph Engel, and Joerg R. Hoerandel. „Cosmic rays from the knee to the highest energies“. In: *Progress in Particle and Nuclear Physics* 63.2 (2009), pp. 293 –338 (cit. on p. 1).

[5]T K Gaisser. „The Cosmic-ray Spectrum: from the knee to the ankle“. In: *Journal of Physics: Conference Series* 47.1 (2006), p. 15 (cit. on p. 1).

[6]G. Giacinti, M. Kachelrieß, and D. V. Semikoz. „Explaining the Spectra of Cosmic Ray Groups above the Knee by Escape from the Galaxy“. In: *Phys. Rev.* D90.4 (2014), p. 041302. arXiv: 1403.3380 [astro-ph.HE] (cit. on p. 2).

[7]Malwina Uellenbeck. „Study of Extragalactic Very High Energy Gamma Ray Sources: Monitoring and Discoveries of Blazars with the MAGIC Telescopes“. PhD thesis. TU Dortmund, 2013 (cit. on pp. 2, 3, 7).

[8]Kenneth Greisen. „End to the Cosmic-Ray Spectrum?“ In: *Phys. Rev. Lett.* 16 (17 1966), pp. 748–750 (cit. on p. 2).

[9]A A Watson. „High-energy cosmic rays and the Greisen–Zatsepin–Kuz'min effect“. In: *Reports on Progress in Physics* 77.3 (2014), p. 036901 (cit. on p. 2).

[10]W.F. Hanlon and The University of Utah. *The Energy Spectrum of Ultra High Energy Cosmic Rays Measured by the High Resolution Fly's Eye Observatory in Stereoscopic Mode*. University of Utah, 2008 (cit. on p. 2).

[11]Heike Prokoph. „Investigations on gamma-hadron separation for imaging Cherenkov telescopes exploiting the time development of particle cascades“. Diplomarbeit. Universitaet Leipzig, 2009 (cit. on pp. 3, 5, 6).

[12]Javier Lopez Munoz. „Measurement of the invariance of the speed of light observing the active galactic nucleus Mkn421 with the MAGIC Telescope“. PhD thesis. Universitat Autonoma de Barcelona, 2006 (cit. on pp. 3, 7, 8).

[13]Boris M Bolotovskii. „Vavilov – Cherenkov radiation: its discovery and application“. In: *Physics-Uspekhi* 52.11 (2009), p. 1099 (cit. on p. 7).

[14]H Anderhub, M Backes, A Biland, et al. „Design and operation of FACT – the first G-APD Cherenkov telescope“. In: *Journal of Instrumentation* 8.06 (2013), P06008 (cit. on p. 7).

[15]Michael Backes. „Long-term observations of the TeV blazar 1ES 1959+650 - Temporal and spectral behavior in the multi-wavelength context“. PhD thesis. TU Dortmund, 2011 (cit. on pp. 8, 11).

[16]A. M. Hillas. „Cerenkov light images of EAS produced by primary gamma“. In: *International Cosmic Ray Conference* 3 (Aug. 1985) (cit. on p. 8).

[17]D. Heck, G. Schatz, T. Thouw, J. Knapp, and J. N. Capdevielle. „CORSIKA: A Monte Carlo code to simulate extensive air showers“. In: (1998) (cit. on p. 10).

[18]H. Anderhub, M. Backes, A. Biland, et al. „FACT—The first Cherenkov telescope using a G-APD camera for TeV gamma-ray astronomy“. In: *Nuclear Instruments and Methods in Physics Research Section A: Accelerators, Spectrometers, Detectors and Associated Equipment* 639.1 (2011). Proceedings of the Seventh International Workshop on Ring Imaging Cherenkov Detectors, pp. 58 –61 (cit. on pp. 11, 12).

[19]Miguel Claro. *http://www.miguelclaro.com/wp/?portfolio=fact-cherenkov-telescope-dragged-milky-way*. 2013 (cit. on p. 11).

[20]A Biland, T Bretz, J Buß, et al. „Calibration and performance of the photon sensor response of FACT — the first G-APD Cherenkov telescope“. In: *Journal of Instrumentation* 9.10 (2014), P10012 (cit. on p. 12).

[21]S. Mueller. „Clear Sight in Cherenkov Astronomy - Investigations of Reflector Geometry and Mirror Alignment for the FACT Telescope“. MA thesis. TU Dortmund, 2014 (cit. on p. 12).

[22]John M. Davies and Eugene S. Cotton. „Design of the quartermaster solar furnace“. In: *Solar Energy* 1.2 (1957), pp. 16 –22 (cit. on p. 12).

[23]K. J. Meier. „FACT - The First G-APD Cherenkov Telescope“. In: (2014) (cit. on p. 13).

[24]A. Moralejo, M. Gaug, E. Carmona, et al. „MARS, the MAGIC Analysis and Reconstruction Software“. In: *ArXiv e-prints* (July 2009). arXiv: `0907.0943 [astro-ph.IM]` (cit. on p. 13).

[25]Dominik Wolfschlaeger. „Development of new image correction method fot the First G-APD Cherenkov Telescope“. B.S. Thesis. RWTH Aachen, 2016 (cit. on pp. 15, 16).

[26]T. Bretz et al. „Comparison of On-Off and Wobble mode observations for MAGIC“. In: *29th International Cosmic Ray Conference Pune* (2005) (cit. on p. 21).

[27]Droege. *Gamma-Ray Astronomy, Influence of wobble positions on the data quality*. URL: `http://www.astro.uni-wuerzburg.de/en/open-projects/fact-open-projects` (visited on Oct. 24, 2016) (cit. on p. 22).

[28]*“private communication”* (cit. on p. 24).

Fig. 7.1: Acronyms

Acronym	Meaning
ASP	Assumed Source Position
CALLISTO	CALibrate LIght Signals and Time Offset
CERES	Camera Electronics and REflector Simulation
COG	Center Of Gravity
CORSIKA	COsmic Ray SImulations for KAscades
DCA	Distance of Closest Approach
DISP	certain distance, see section 2.2.1
DIST	certain distance, see section 2.2.1
EAS	Extended Air Shower
FACT	First G-APD Cherenkov Telescope
GANYMED	Gmmas Are Now Your Most Exciting Discovery
G-APD	Geiger-mode Avalanche PhotoDiode
IACT	Imaging Atmospheric Cherenkov Telescope
MAGIC	Major Atmospheric Gamma-Ray Imaging Cherenkov Telescopes
MARS	MAGIC Analysis and Reconstruction Software
MARS CheObs ed.	Modular Analysis and Reconstruction Software - Cherenkov Oberservation Edition
RMS	Root-Mean Square
RSP	Reconstructed Source Position
slope	SlopeLong (see section 2.2.1
SPONDE	SPectrum ON DEmand
STAR	STandard Analysis and Reconstruction
VHE	Very High Energy
W/L	Width-to-Length ratio

Appendix

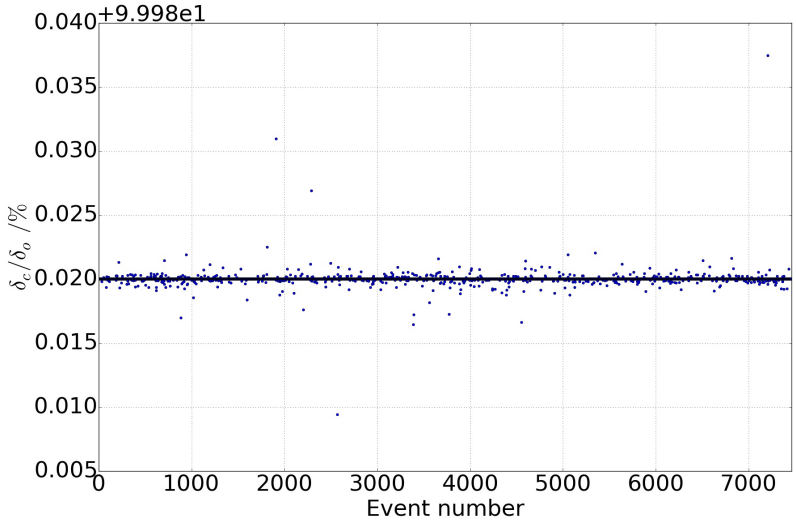

Fig. 7.2: Relative change of δ for 7463 considered events, $\overline{\delta_c/\delta_o} = 0.999999 \pm 0.000003$. No correction is expected.

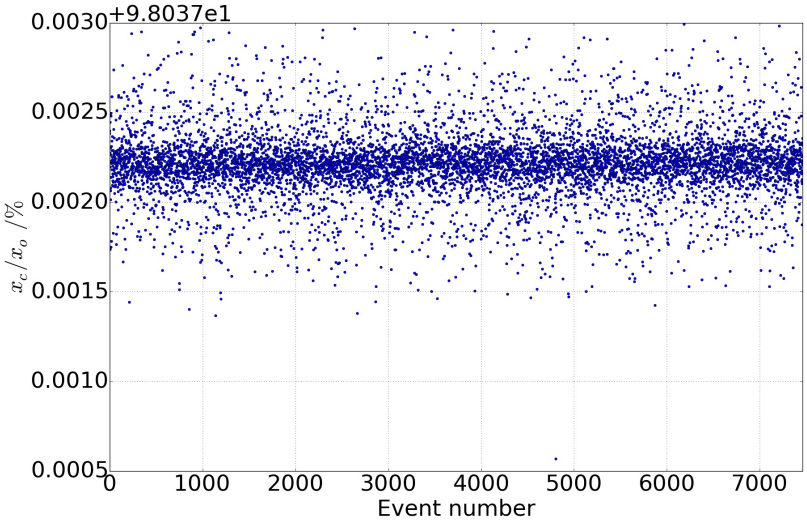

Fig. 7.3: Relative change of x-coordinate of COG for 7464 considered events, $\overline{\mathrm{x}_c/\mathrm{x}_o} = 0.980392 \pm 0.000002$. Adjustment of ≈ 0.980392 is expected.

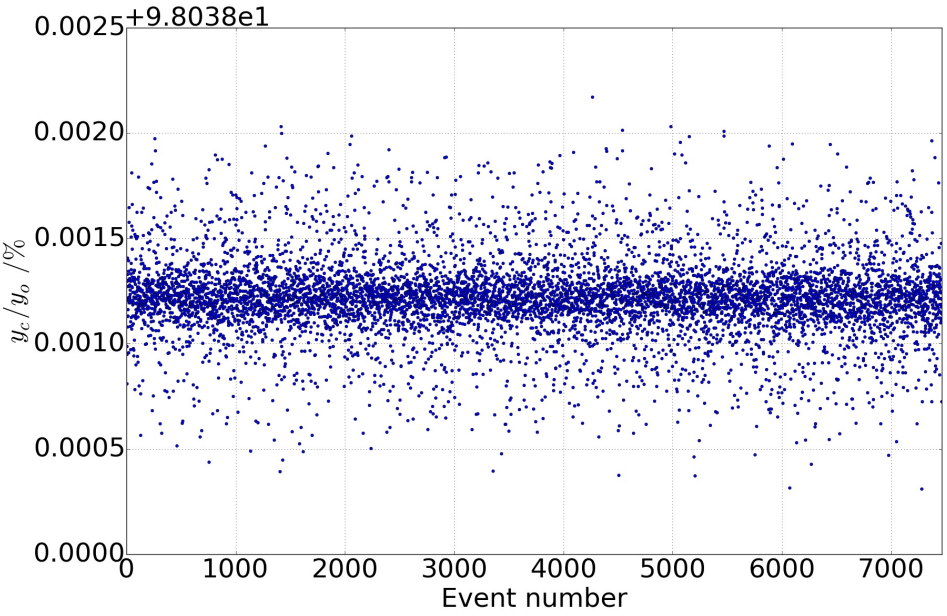

Fig. 7.4: Relative change of y-coordinate of COG for 7464 considered events, $\overline{\mathrm{y}_c/\mathrm{y}_o} = 0.980392 \pm 0.000002$. Adjustment of ≈ 0.980392 is expected.

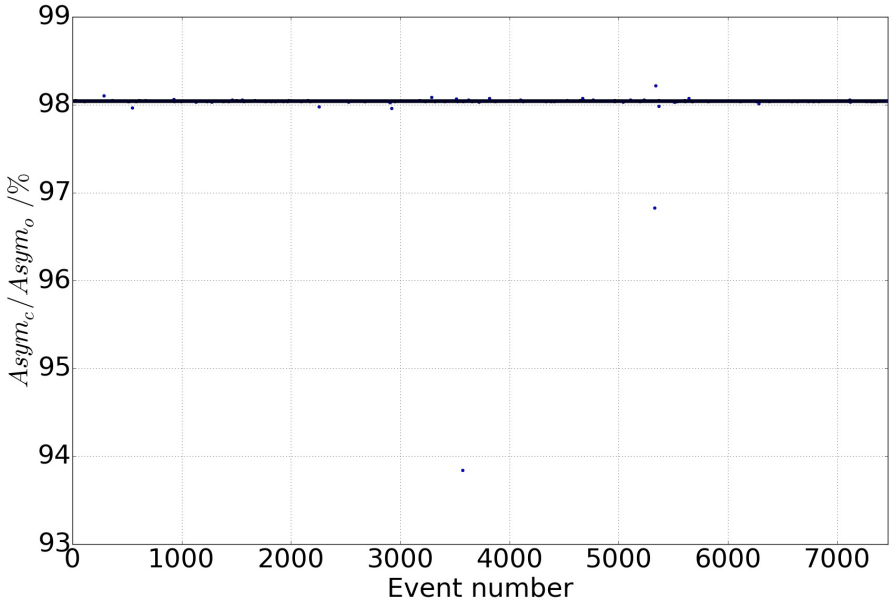

Fig. 7.5: Relative change of Asym for 7464 considered events, $\overline{\mathrm{Asym}_c/\mathrm{Asym\_o}} = 0.9804 \pm 0.0005$. Adjustment of ≈ 0.9804 is expected.

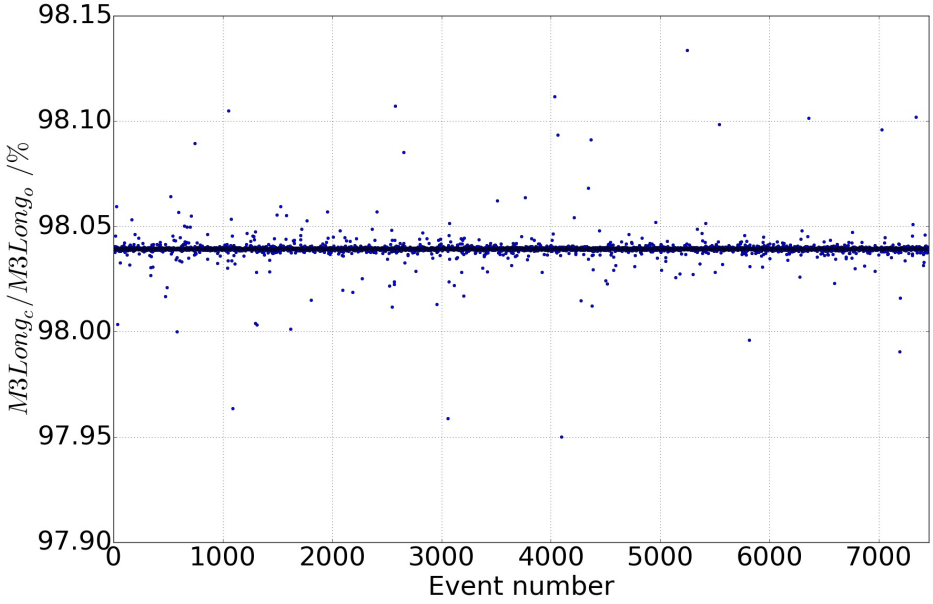

Fig. 7.6: Relative change of M3Long for 7457 considered events, $\overline{\text{M3Long}_c/\text{M3Long}_o} = 0.98039 \pm 0.00004$. Adjustment of ≈ 0.98039 is expected.

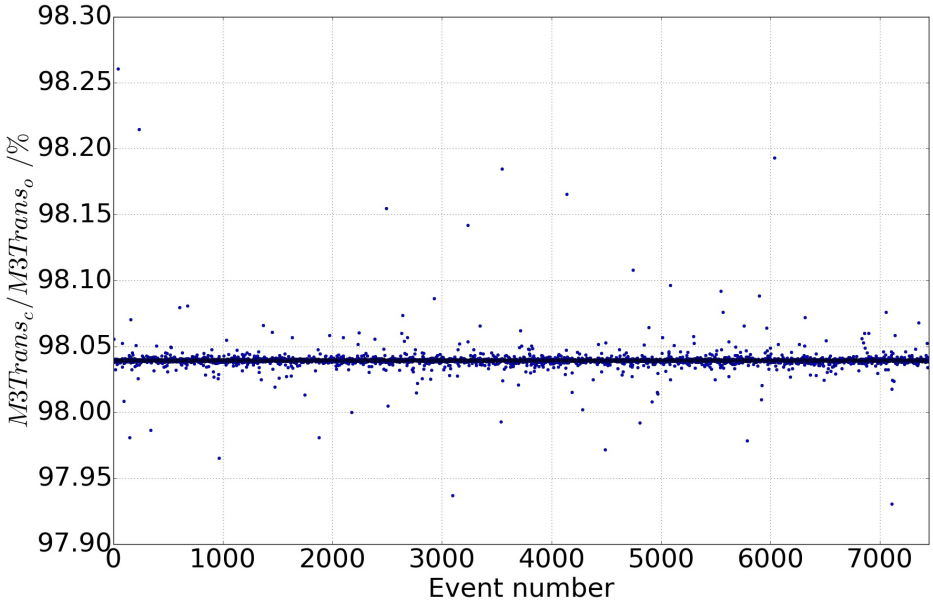

Fig. 7.7: Relative change of M3Trans for 7446 considered events, $\overline{\text{M3Trans}_c/\text{M3Trans}_o} = 0.98039 \pm 0.00006$. Adjustment of ≈ 0.98039 is expected.

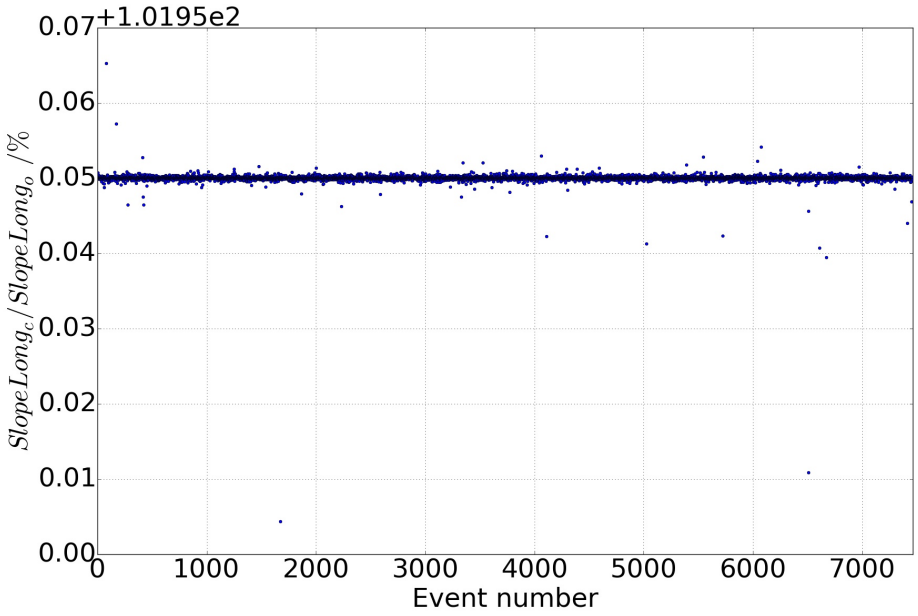

Fig. 7.8: Relative change of SlopeLong for 7464 considered events, $\overline{\text{SlopeLong}_c/\text{SlopeLong}_o} = 1.019999 \pm 0.000008$. Adjustment of ≈ 1.02 is expected.

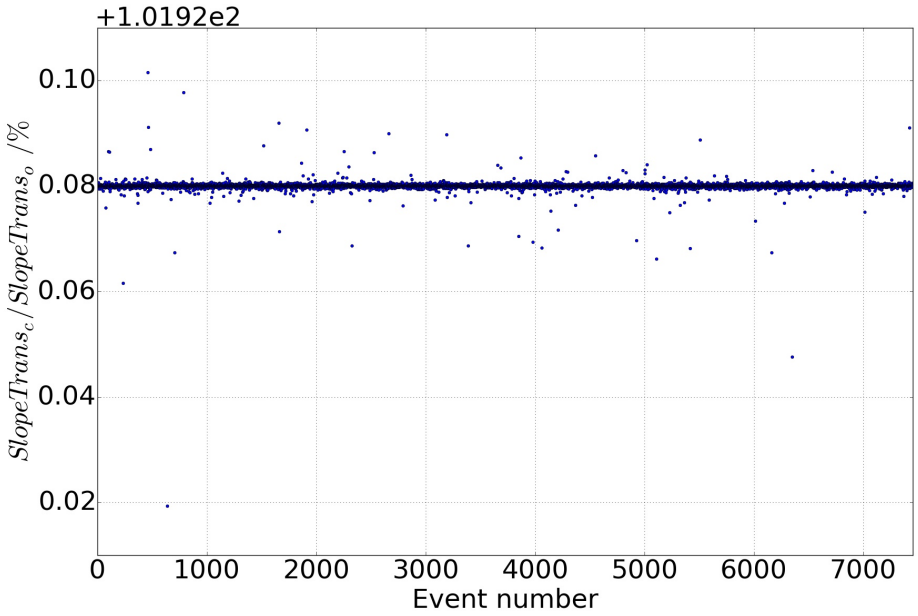

Fig. 7.9: Relative change of SlopeTrans for 7454 considered events, $\overline{\text{SlopeTrans}_c/\text{SlopeTrans}_o} = 1.01999 \pm 0.00001$. Adjustment of ≈ 1.02 is expected. SlopeTrans can feature some large values since some showers are strongly compressed along the minor axis. Those events are not considered.

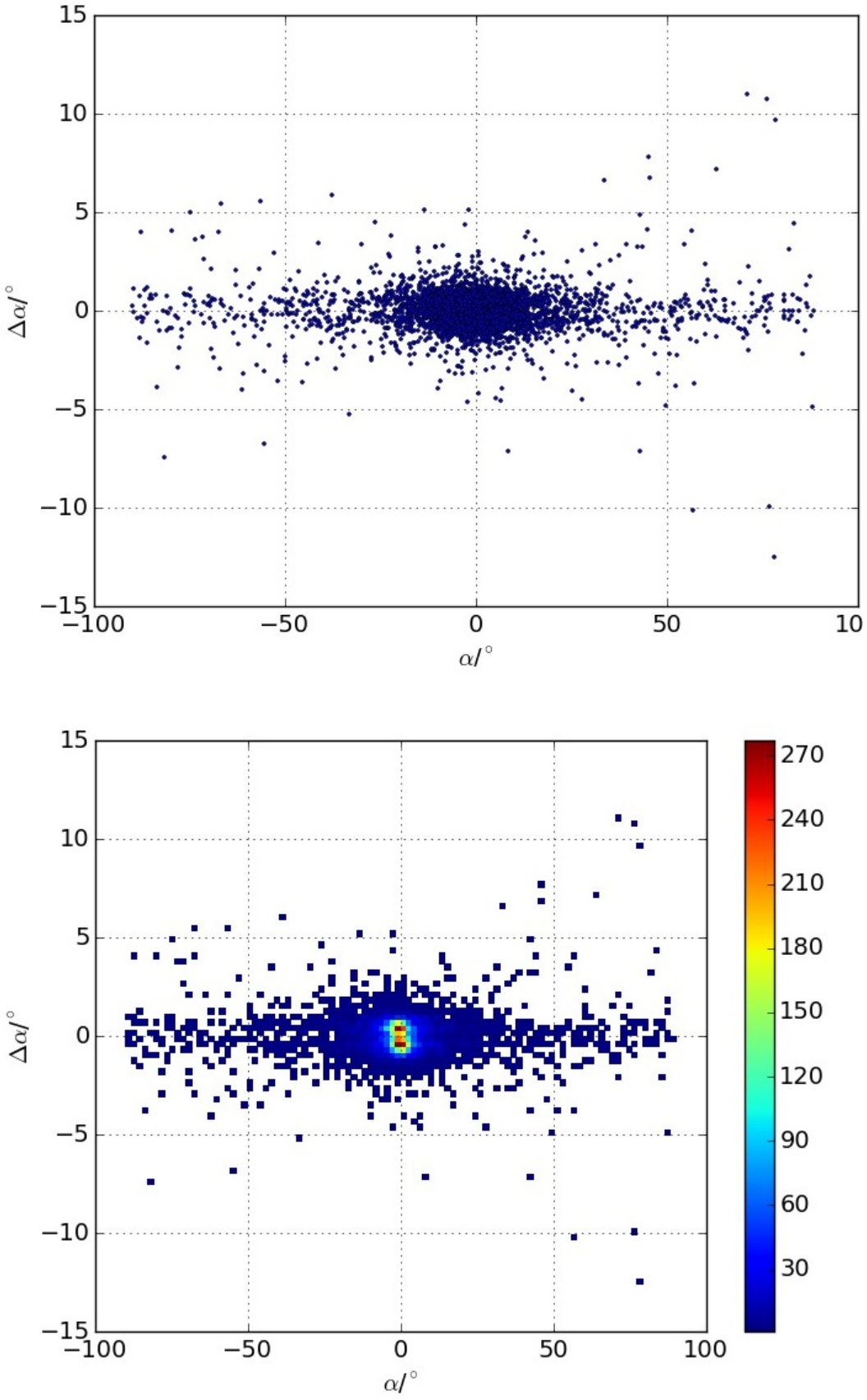

Fig. 7.10: Distribution of $\Delta\alpha$, 7622 events. Statistically distributed around x-axis.

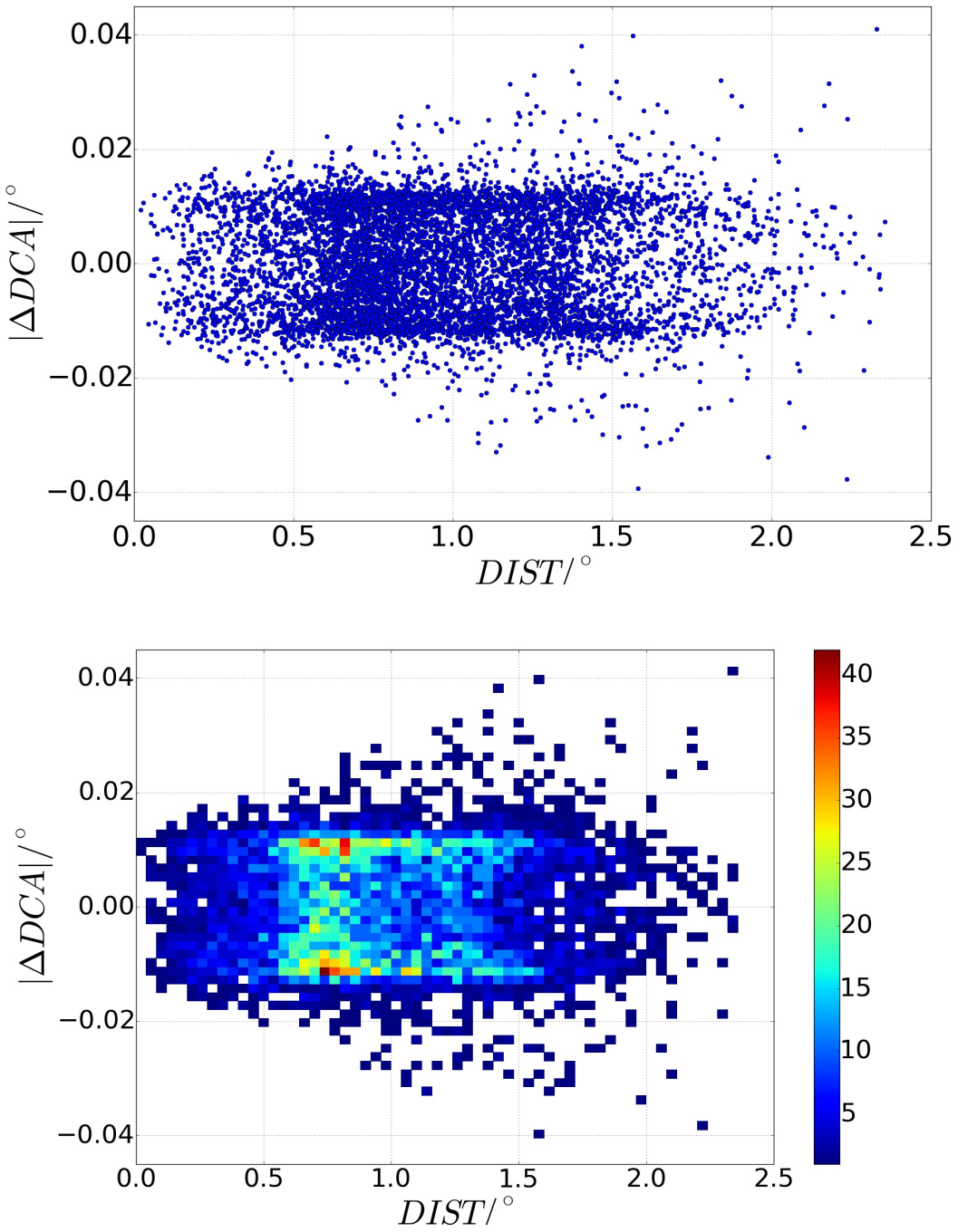

Fig. 7.11: Distribution of ΔDCA, 7622 events. Statistically distributed around x-axis.

Listing 7.1: Compressed source-code MHillas::Calc() with image correction implemented, bold lines are relevant for correction.

```
Int_t MHillas::Calc(const MGeomCam &geom, const MSignalCam &evt,
 Int_t island, Float_t fAberration)
{
    const UInt_t numpix  = evt.GetNumPixels();
    //
    // sanity check 1 (special MC events)
    //
    if (numpix==0)
        return 1;
    //
    // calculate mean value of pixel coordinates and fSize
    // ---------------------------------------------------
    //
    // Because this are only simple sums of roughly 600 values
    // with an accuracy less than three digits there should not
    // be any need to use double precision (Double_t) for the
    // calculation of fMeanX, fMeanY and fSize.
    //
    fMeanX = 0;
    fMeanY = 0;
    fSize  = 0;
    UInt_t numused = 0;

    for (UInt_t i=0; i<numpix; i++)
    {
        MSignalPix &pix = evt[i];
        if (!pix.IsPixelUsed())
            continue;
        if (island>=0 && pix.GetIdxIsland()!=island)
            continue;
        const MGeom &gpix = geom[i];
        const Float_t nphot = pix.GetNumPhotons();
        fSize  += nphot;                          // [counter]
        fMeanX += nphot * fAberration * gpix.GetX(); // [mm]
        fMeanY += nphot * fAberration * gpix.GetY(); // [mm]
        numused++;
    }
    // sanity check 2
    if (fSize==0)
        return 2;
```

```
    fMeanX /= fSize;                                    // [mm]
    fMeanY /= fSize;                                    // [mm]
    //
    // sanity check 3
    //
    if (numused<3)
        return 3;
    //
    // calculate 2nd moments
    // ----------------------
    //
    // To make sure that the more complicated sum is evaluated as
    // accurate as possible (because it is needed for more
    // complicated calculations (see below) we calculate it using
    // double prcision.
    //
    Double_t corrxx=0;                                  // [m^2]
    Double_t corrxy=0;                                  // [m^2]
    Double_t corryy=0;                                  // [m^2]
    for (UInt_t i=0; i<numpix; i++){
        const MSignalPix &pix = evt[i];
        if (!pix.IsPixelUsed())
            continue;
        if (island>=0 && pix.GetIdxIsland()!=island)
            continue;
        const MGeom &gpix = geom[i];
        const Float_t dx = fAberration * gpix.GetX() - fMeanX;
        const Float_t dy = fAberration * gpix.GetY() - fMeanY;
        const Float_t nphot = pix.GetNumPhotons();
        corrxx += nphot * dx*dx;                // [mm^2]
        corrxy += nphot * dx*dy;                // [mm^2]
        corryy += nphot * dy*dy;                // [mm^2]
    }
```

```
    // calculate the basic Hillas parameters: orientation
    // and size of axes
    // ------------------------------------------------------
    // fDelta is the angle between the major axis of the
    // ellipse and the x axis. It is independent of the position
    // of the ellipse in the camera it has values between -pi/2
    // and pi/2 degrees
    const Double_t d0    = corryy - corrxx;
    const Double_t d1    = corrxy*2;
    const Double_t d2    = TMath::Sqrt(d0*d0 + d1*d1) + d0;
    const Double_t tand  = d2==0 ? 0 : d2 / d1;
    const Double_t tand2 = tand*tand;
    const Double_t s2    = tand2+1;
    const Double_t s     = TMath::Sqrt(s2);
    // Set default for the case in which the image is symmetric
    // on the y-axis
    fDelta    = TMath::Pi()/2;
    fCosDelta = 0;
    fSinDelta = 1;
    Double_t axis1 = corryy;
    Double_t axis2 = corrxx;
    // This are all cases in which the image is not symmetric
    // on the y-axis
    if (d1!=0 || d2==0){
        fDelta    = TMath::ATan(tand);
        fCosDelta = 1.0 /s;   // need these in derived classes
        fSinDelta = tand/s;   // like MHillasExt
        axis1 = (tand2*corryy + d2 + corrxx)/s2;
        axis2 = (tand2*corrxx - d2 + corryy)/s2;
    }
    //
    // fLength^2/fWidth^2 is the second moment along the
    // major/minor axis of the distribution
    // From the algorithm we get: fWidth <= fLength is always true
    //
    // very small numbers can get negative by rounding
    //
    fLength = axis1<0 ? 0 : TMath::Sqrt(axis1/fSize);//[mm]
    fWidth  = axis2<0 ? 0 : TMath::Sqrt(axis2/fSize);//[mm]
    SetReadyToSave();
    return 0;
}
```

Listing 7.2: Compressed source-code MHillasExt::Calc with image correction implemented, bold lines are relevant for correction.

```
Int_t MHillasExt::Calc(const MGeomCam &geom,
const MSignalCam &evt, const MHillas &hil,
Int_t island, Float_t fAberration)
{
    //  calculate the additional image parameters
    // ------------------------------------------------
    // loop to get third moments along ellipse axes and
    // two max pixels. For the moments double precision
    // is used to make sure, that the complex matrix
    // multiplication and sum is evaluated correctly.
    Int_t maxpixid  = 0;
    Float_t maxpix  = 0;

    // Variables to caluclate time slope
    // Formula: http://mo.mathematik.uni-stuttgart.de...
    // .../inhalt/erlaeuterung/erlaeuterung300/
    UInt_t cnt = 0;

    Double_t sumx      = 0;
    Double_t sumy      = 0;
    Double_t sumt      = 0;
    Double_t sumw      = 0;

    Double_t sumxt     = 0;
    Double_t sumyt     = 0;

    Double_t sumx2     = 0;
    Double_t sumy2     = 0;
    Double_t sumxy     = 0;
    Double_t sumt2     = 0;

    Double_t sumxw     = 0;
    Double_t sumyw     = 0;
    Double_t sumtw     = 0;

    Double_t sumx2w    = 0;
    Double_t sumy2w    = 0;
    Double_t sumt2w    = 0;
```

```
        Double_t sumxyw    = 0;
40      Double_t sumxtw    = 0;
        Double_t sumytw    = 0;

        Double_t sumdx3w   = 0;
        Double_t sumdy3w   = 0;
45
        Double_t sumdx2dyw = 0;
        Double_t sumdxdy2w = 0;

        const UInt_t npix = evt.GetNumPixels();
50      for (UInt_t i=0; i<npix; i++)
        {
            const MSignalPix &pix = evt[i];
            if (!pix.IsPixelUsed())
                continue;
55
            if (island>=0 && pix.GetIdxIsland()!=island)
                continue;

            const MGeom &gpix = geom[i];
60
            const Double_t x = fAberration * gpix.GetX();
            const Double_t y = fAberration * gpix.GetY();
            const Double_t t = pix.GetArrivalTime();

65          Double_t nphot = pix.GetNumPhotons();         // [1]

            // --- time slope ---
            sumx    += x;
            sumy    += y;
70          sumt    += t;
            sumw    += nphot;

            sumxt   += x*t;
            sumyt   += y*t;
75
            sumx2   += x*x;
            sumy2   += y*y;
            sumxy   += x*y;
            sumt2   += t*t;
```

```
        sumxw   += x*nphot;
        sumyw   += y*nphot;
        sumtw   += t*nphot;

        sumx2w  += x*x*nphot;
        sumy2w  += y*y*nphot;
        sumt2w  += t*t*nphot;

        sumxyw  += x*y*nphot;

        sumxtw  += x*t*nphot;
        sumytw  += y*t*nphot;

        // --- 3rd moment ---
        const Double_t dx = x - hil.GetMeanX();      // [mm]
        const Double_t dy = y - hil.GetMeanY();      // [mm]

        sumdx3w   += dx*dx*dx*nphot;
        sumdy3w   += dy*dy*dy*nphot;
        sumdx2dyw += dx*dx*dy*nphot;
        sumdxdy2w += dx*dy*dy*nphot;

        cnt++;

        //
        // Now we are working on absolute values of nphot, which
        // must take pixel size into account
        //
        nphot *= geom.GetPixRatio(i);

        // --- max pixel ---
        if (nphot>maxpix)
        {
            maxpix   = nphot;
            maxpixid = i;
        }
    }

    const Double_t c = hil.GetCosDelta();
    const Double_t s = hil.GetSinDelta();
```

```
        //
        // Time slope
        //
        const Double_t dxt  =  c*sumxt + s*sumyt;
125     const Double_t dyt  = -s*sumxt + c*sumyt;

        const Double_t dx   =  c*sumx  + s*sumy;
        const Double_t dy   = -s*sumx  + c*sumy;

130     const Double_t dx2  =  c*c*sumx2 + 2*c*s*sumxy + s*s*sumy2;
        const Double_t dy2  =  s*s*sumx2 - 2*c*s*sumxy + c*c*sumy2;

        const Double_t detx =  cnt*dx2 - dx*dx;
        const Double_t dety =  cnt*dy2 - dy*dy;
135
        fSlopeLong  = detx==0 ? 0 : (cnt*dxt - sumt*dx)/detx;
        fSlopeTrans = dety==0 ? 0 : (cnt*dyt - sumt*dy)/dety;

        //
140     // Time spread
        //
        const Double_t m = fSlopeLong;

        const Double_t z        = dx; //c*sumx   + s*sumy;
145     const Double_t zw       =       c*sumxw  + s*sumyw;

        const Double_t zt       = dxt; //c*sumxt  + s*sumyt;
        const Double_t ztw      =        c*sumxtw + s*sumytw;

150     const Double_t x2y2     = dx2;
        const Double_t x2y2w    = c*c*sumx2w + s*s*sumy2w + 2*c*s*sumxyw;

        const Double_t sumdt    = sumt  - m*z;
        const Double_t sumdtw   = sumtw - m*zw;
155
        const Double_t sumdt2   = sumt2  + m*m*x2y2  - 2*m*zt;
        const Double_t sumdt2w  = sumt2w + m*m*x2y2w - 2*m*ztw;

        const Double_t meant    = sumt  /cnt;
160     const Double_t meandt   = sumdt /cnt;
        const Double_t meantw   = sumtw /sumw;
        const Double_t meandtw  = sumdtw/sumw;
```

```
    fTimeSpread = TMath::Sqrt(sumt2 /cnt  - meant *meant);
    fTimeSpreadWeighted = TMath::Sqrt(sumt2w/sumw - meantw*meantw);

    fSlopeSpread = TMath::Sqrt(sumdt2 /cnt  - meandt *meandt);
    fSlopeSpreadWeighted=TMath::Sqrt(sumdt2w/sumw–meandtw*meandtw);

    // Third moments along axes get normalized
    //
    const Double_t m3l = c*c*c*sumdx3w + s*s*s*sumdy3w
                       + 3*(s*c*c*sumdx2dyw + c*s*s*sumdxdy2w);
    const Double_t m3t = c*c*c*sumdy3w - s*s*s*sumdx3w
                       + 3*(s*s*c*sumdx2dyw - s*c*c*sumdxdy2w);
    fM3Long  = MMath::Sqrt3(m3l/sumw);      // [mm]
    fM3Trans = MMath::Sqrt3(m3t/sumw);      // [mm]

    // Asymmetry
    const MGeom &maxp = geom[maxpixid];
    fAsym = (hil.GetMeanX()-fAberration * maxp.GetX())*c
          + (hil.GetMeanY()- fAberration * maxp.GetY())*s;

    SetReadyToSave();
    return 0;
  }
```